Water Resources Research

RESEARCH ARTICLE
10.1029/2023WR035098

The Overall Collection Efficiency of Catching-Type Precipitation Gauges in Windy Conditions

A. Cauteruccio[1,2], E. Chinchella[1,2], and L. G. Lanza[1,2]

[1]Department of Civil, Chemical and Environmental Engineering, University of Genova, Genova, Italy, [2]WMO Measurement Lead Centre "B. Castelli" on Precipitation Intensity, Genova, Italy

Key Points:

- The wind induced bias of six common precipitation gauges is quantified using Computational Fluid Dynamics with embedded particle tracking
- Overall collection efficiency trends with precipitation intensity show that the gauge performance varies according to its outer geometry
- Results allow selecting appropriate gauge models for the local precipitation climatology and applying adjustments to the measured data

Correspondence to:

A. Cauteruccio,
arianna.cauteruccio@edu.unige.it

Citation:

Cauteruccio, A., Chinchella, E., & Lanza, L. G. (2024). The overall collection efficiency of catching-type precipitation gauges in windy conditions. *Water Resources Research*, *60*, e2023WR035098. https://doi.org/10.1029/2023WR035098

Received 12 APR 2023
Accepted 22 DEC 2023

Author Contributions:

Conceptualization: A. Cauteruccio, E. Chinchella, L. G. Lanza
Data curation: E. Chinchella
Formal analysis: A. Cauteruccio
Investigation: A. Cauteruccio, E. Chinchella, L. G. Lanza
Methodology: A. Cauteruccio, E. Chinchella, L. G. Lanza
Software: E. Chinchella
Supervision: L. G. Lanza
Visualization: A. Cauteruccio, E. Chinchella, L. G. Lanza
Writing – original draft: A. Cauteruccio
Writing – review & editing: A. Cauteruccio, E. Chinchella, L. G. Lanza

Abstract The wind-induced bias of catching-type precipitation measurement instruments is quantified using Computational Fluid Dynamics with embedded liquid (raindrops) and solid (snowflakes) particle tracking. The performance of six common commercial gauges having different outer geometry is compared under a range of Precipitation Intensity (PI) and wind speed conditions by means of the numerically calculated catch ratios. Validation of the simulated aerodynamic behavior and its effect on water drop trajectories is provided by previous wind tunnel experiments. The functional dependence of the overall collection efficiency on the PI is derived as a quantitative measure of the instrument performance under a wind climatology with a uniform probability density function. Instruments with aerodynamic design produce a less pronounced diversion of hydrometeor trajectories—at any given size—than those having more traditional geometry. For liquid precipitation measurements, chimney-shaped instruments rank low, while inverted conical and Nipher shielded instruments are quite performant solutions. The investigated quasi-cylindrical gauges have intermediate behavior depending on their detailed aerodynamic features. For solid precipitation, all instruments rank low at light to moderate PI, except the Nipher shielded gauge. Results allow selecting the appropriate instrument for the local precipitation climatology at the measurement site and can be used to apply suitable adjustments to the measured precipitation.

1. Introduction

In situ measurement of liquid and solid atmospheric precipitation in windy conditions is still a challenging task even for the most advanced automatic instrumentation (Cauteruccio, Colli, et al., 2021). Further to the instrumental bias (minimized in case of accurate instrument calibration), various environmental sources of bias, including siting issues and exposure, affect the measurement accuracy. As reported by Rodda and Dixon (2012), the work of Kurtyka (1953) already showed that wind is by far the most impactful environmental source of bias, outperforming by 3–50 times the total impact of all other environmental factors.

The literature extensively reports of the wind-induced bias observed when comparing precipitation measurements from multiple locations having wind climatology differences (Pollock et al., 2018) and between shielded and unshielded instrument configurations (see e.g., Colli et al., 2016a, 2016b; Duchon & Essenberg, 2001). The impact of the resulting bias on derived variables was also recognized and documented for example, by Rodda and Smith (1986) who noted that the deposited acidity values of precipitation can be larger by up to 20% and more than those reported based on the UK standard gauge measurements in case of wind.

This well-understood measurement bias (also known as the exposure problem) arises from the bluff-body aerodynamic behavior of the measurement instrument itself, when exposed to the wind. The obstruction produced by the instrument body against the wind generates significant airflow acceleration and vertical velocity components able to deviate the approaching hydrometeors from their undisturbed trajectory, away from the instrument collector. The pattern and numerosity of the deviated trajectories mainly depend (further to the relevant environmental factors) on the instrument geometry, and generally result in some undercatch of the precipitation amount with respect to what would be collected in the absence of wind.

The first assessment of the aerodynamic effect in precipitation measurements is generally attributed to Jevons (1861), who noted that the instrument "is itself an obstacle, causing the wind to swerve aside, and to change the direction in which the raindrops fall." Jevons was addressing the difference in precipitation measurements observed by instruments located at different elevations above the ground level, especially when sited on a rooftop or a tower, and suggested that only installing the instrument with the collector leveled with the

surrounding ground would avoid any wind-induced undercatch. After Koshmieder (1934), the wind exposure problem is also termed the "Jevons effect," and a standard pit gauge (CEN, 2010) was developed as a reference installation for liquid precipitation based on Jevons' recommendations.

However, Jevons himself referred to some previous work, especially by Meikle (1819) who already stated: "I can hardly pretend to give a complete solution of this well-known paradox," (i.e., the increased precipitation measured by gauges sited at low elevation with respect to those sited at high elevation) "but am disposed to think it is in some way owing to the obstruction which the gauge itself offers to the wind. Perhaps the winds being made to rush with greater rapidity, and a little upward in beginning to pass over the mouth of the gauge, prevents the rain from falling into that part of it which is next the wind." Jevons attributed a lower relevance to the obstruction given by the instruments than to the presence of other types of obstacles such as buildings, vegetation, or the local topography. The first author to notice the aerodynamic influence (bluff-body behavior) of the gauge on the catch performance was therefore Meikle (1819).

Quantitatively, according to Sevruk (1982), the wind-induced undercatch for liquid precipitation measurements can be estimated within 2%–10%, while Pollock et al. (2018) reported an observed undercatch of about 10%–23% from field experiments performed at a lowland (scarce wind) and upland (strong wind) site, respectively. Duchon and Essenberg (2001) reported a mean undercatch bias of 4% after comparing pit and aboveground low-elevation rain gauges with and without wind shields. Muchan and Dixon (2019) found a magnitude of the undercatch bias equal to 12.7% in a field test study, while Utsumi et al. (2008) reported an increase of daily precipitation of about 10% after accounting for the wind-induced undercatch in a nation-wide rainfall climatology study in Japan.

Yang et al. (1999) reported experimental results for the Hellmann non-recording gauge obtained at four different stations in Finland, Russia, Germany, and Croatia, with percentage undercatch biases of about 10% for liquid-, 25% for mixed-, and 50% for solid precipitation. Rasmussen et al. (2012) and Colli et al. (2015) show collection losses for solid precipitation even reaching 70%–80% from a field test site in Colorado, US. The extensive, multiple site campaign of the Solid Precipitation InterComparison Experiment (SPICE)—held by the World Meteorological Organization (WMO)—reported of a large impact of wind on the measured solid precipitation with an estimated undercatch approaching 80% in the wind speed range between 4 and 6 m s^{-1} (Nitu et al., 2018). Masuda et al. (2019) applied different adjustment methods to the mean monthly precipitation yielding an increase in the winter (December–February) precipitation amount in Japan by 12.7%, while the discrepancy between precipitation and runoff/evapotranspiration in the annual hydrological balance was reduced from 33% to 26% over the mountainous terrain.

Further to the instrument geometry, the wind-induced bias was shown to depend (e.g., by Thériault et al., 2012) on the microphysical characteristics of hydrometeors and the particle size distribution (PSD). More recently, the physical dependence of the undercatch bias on the measured PI was demonstrated by Colli et al. (2020) for solid precipitation and by Cauteruccio and Lanza (2020) for liquid precipitation. This result was later confirmed by Leroux et al. (2021) and Hoover et al. (2021), who found a dependence of the undercatch bias on the hydrometeor fall velocity, being the fall velocity in the atmosphere basically controlled by the size (and shape) of the falling particles, therefore by the PI itself.

Adjustments to account for the wind-induced bias have been proposed in the literature, mostly based on in-field and/or wind tunnel experiments (see e.g., Mueller & Kidder, 1972; Wolff et al., 2015) and numerical simulation (see e.g., Nešpor & Sevruk, 1999; Thériault et al., 2012). To adjust the measured precipitation and match the amount that would be measured by a reference installation under the same wind conditions, various transfer functions were also developed (see e.g., Kochendorfer et al., 2018). The transfer functions proposed within the WMO SPICE and more recent follow-up developments are described in Kochendorfer et al. (2022) and the references therein. Chubb et al. (2015) applied different transfer functions to a series of precipitation measurements in Australia with improvements between 3% and 52% over the unadjusted precipitation. Smith et al. (2022) applied transfer functions limited to undercatch values of 50%–60% to accumulated precipitation measurements at the hourly scale in a Canadian nationwide study.

A comprehensive assessment of the performance of the most common and commercially available instruments for both liquid and solid precipitation is however still lacking due to the difficulty of testing the instruments in the field under a variety of instrument shape, PI and wind speed combinations. These are indeed hardly observed within (even long-term) in-field experimental campaigns due to the specific local climatology of

Table 1
Geometrical Characteristics of the Investigated Instruments

Instrument	External geometry	Collector diameter, Φ (mm)	Collector area (cm^2)	Height (cm)	Measurement principle
CH-GEO	Chimney	160	200	74	Weighing
CH-OTT	Chimney	160	200	75.7	Weighing
CY-CAE	Cylindrical	357	1,000	60	Tipping-bucket
CY-LAM	Cylindrical	162	200	30.7	Weighing
IC-EML	Inverted conical	251	500	42.5	Tipping-bucket
SH-AES	Shielded	121	150	59.8	Totalizer

any single test site. Numerical simulation of the wind-induced measurement bias based on Computational Fluid Dynamics (CFD) with embedded particle tracking is a viable solution to overcome such difficulties (see e.g., Colli et al., 2016a, 2016b; Folland, 1988; Nešpor & Sevruk, 1999; Thériault et al., 2012), although comprehensive studies involve a significant computational burden. A detailed comparison of numerical results for instruments with various outer shapes was proposed by Colli et al. (2018) but the study was limited to the analysis of their aerodynamic performance, with no quantitative information about the associated measurement bias.

In this work, we quantify and compare for the first time the performance of six different precipitation measurement instruments (with shapes that are representative of the most common geometries commercially available at the time of writing), numerically simulated under a wide range of PI and wind speed conditions. The investigated models (with the short name adopted in the following) are the Geonor T-200B chimney-shaped, weighing gauge (named CH-GEO), the OTT Pluvio^2 chimney-shaped, weighing gauge (named CH-OTT), the CAE PG10 quasi-cylindrical, tipping-bucket gauge (named CY-CAE), the Lambrecht rain[e]H3 cylindrical, weighing gauge (named CY-LAM), the EML SBS500 inverted conical, tipping-bucket gauge (named IC-EML), and the AES Nipher shield containing a totalizer gauge, that is a cylindrical vessel that collects the cumulated precipitation (named SH-AES). Table 1 reports the relevant geometrical characteristics of the investigated instruments, with Φ the collector's diameter. Images of the gauges are presented in the supplementary material (Chinchella et al., 2023).

The choice of instruments aimed at considering three pairs of gauges, each with similar geometrical characteristics, to represent most instruments that are presently available on the market. In this work no add-on wind shields were considered, like the Alter shield (Alter, 1937) or the Double Fence Intercomparison Reference adopted by the WMO, since the numerical simulation of the wind-induced bias for shielded gauges is widely addressed in the literature (see e.g., Colli et al., 2016a, 2016b; Thériault et al., 2015). Furthermore, such shields are commonly used in experimental sites, mainly for research purposes, and their use is less common in urban area installations and for large networks due to their cost and relatively larger footprint. The only shielded gauge (SH-AES) was included in the performed comparison since it is integrated and compact and is a good representative instrument for the category of aerodynamic gauges.

The analysis is limited to catching type instruments, that is, those equipped with a collector to convey precipitation into a container, since they are the most widely used in operational monitoring networks. Non-catching instruments and disdrometers used to measure precipitation are subject to wind-induced biases as well (see e.g., Chinchella et al., 2021; Nešpor et al., 2000), although their non-axially symmetric design (involving the wind direction as an additional influencing factor) and their specific (often optical) measuring principles make the quantification of such biases, and the resulting adjustments, quite a challenging task.

2. Methodology

A numerical simulation approach is adopted to cover a comprehensive set of multiple instrument shape, wind speed, hydrometeor type and PI combinations. Resorting to a CFD modeling approach with embedded liquid and solid particle tracking algorithms allows simulating both the aerodynamic behavior of each instrument and the resulting collection performance. The approach, originally proposed by Nešpor and Sevruk (1999), and improved

by Colli et al. (2015) is described in Cauteruccio, Chinchella, et al. (2021) for solid precipitation and in Cauteruccio et al. (2021b) for liquid precipitation.

A time independent scheme is used, based on the numerical solution of the Unsteady Reynold Averaged Navier-Stokes (URANS) equations (Reynolds, 1895), derived from the Navier-Stokes (NS) and the continuity equations for an incompressible fluid. The model provides information about the flow after a steady state condition is reached and in the hypothesis of stationary turbulence characteristics, solving the average part of the flow variables while modeling the turbulence induced fluctuations.

The k-ω shear stress transport turbulence model developed by Menter (1994) and slightly revised in Menter et al. (2003) is implemented, with k the turbulent kinetic energy and ω the specific turbulent dissipation rate. This model combines the excellent performance of the baseline k-ω model, developed by Wilcox (1988), near the solid boundary walls (where velocity values are fixed) with the stability of the k-ε model (with ε the turbulence dissipation ratio), proposed by Jones and Launder (1972), in the free stream. The zonal formulation is reconciled by means of suitable blending functions.

The numerical solution of the URANS equations is obtained using the OpenFOAM (Open Field Operation And Manipulation) software—an open source C++ modeling toolbox for fluid dynamics related problems (Chen et al., 2014), using the PIMPLE solver algorithm. Coupling PIMPLE with a pseudo-transient approach based on a local time stepping numerical scheme (Jeanmasson et al., 2019) allows reducing considerably the computational burden. In this approach, the simulation is forced toward a steady state condition similarly to the Reynolds-averaged Navier–Stokes approach, but with no need to remove the time derivative in the NS equations, therefore improving stability especially for complex geometries.

Simulations are conducted by setting air as an incompressible fluid, with a density of 1.0 kg m^{-3} and a kinematic viscosity of 1.5×10^{-5} m^2 s^{-1}. From preliminary simulations the dimensionless wall distance (y+) is evaluated. Using this variable, a "law of the wall" (Spalding, 1961) was experimentally defined, which describes the non-dimensional velocity profile inside a turbulent boundary layer. Depending on the wind velocity, its average value indicates whether the grid cells closest to the instrument surface are positioned in the buffer or in the log-law layer. Appropriate wall functions (independent on y+, see Spalding, 1961) are used for k, ω, and the turbulent viscosity (ν_t) as near-wall boundary conditions at all solid surfaces (Liu, 2016).

Hydrometeor trajectories are modeled using a Lagrangian Particle Tracking (LPT) algorithm, embedded in OpenFOAM. Multiple independent particles are released in the airflow field and both the particle displacement and the possible impact location at selected boundaries are calculated. Since the volume fraction of hydrometeors in precipitation events is generally low even at high precipitation rates (Uijlenhoet & Torres, 2006), particle-to-particle interactions can be neglected, at least close to the ground where precipitation gauges are positioned. It is also assumed that turbulence-induced interactions between small and large drops close to the gauge body are rare and the resulting effect is negligeable. An uncoupled LPT model is therefore used to simulate natural precipitation, where the flow field is unaffected by the presence of the particles and particle-to-particle interactions are rare, and trajectories are computed from a static velocity field (the steady state solution).

Validation is essential to substantiate the results of any simulation approach, and the adopted numerical setup was extensively validated in previous studies by means of dedicated wind tunnel experiments. For the validation of the airflow simulation setup, the reader is referred to the wind tunnel experiments previously published by Cauteruccio et al. (2020, 2021a) using flow velocity probes and Particle Image Velocimetry. The efficacy of the LPT model for liquid precipitation was validated by Cauteruccio et al. (2021b) by injecting water drops in the wind tunnel and measuring their trajectories with a high-speed camera. For solid precipitation, the validation of the numerical approach (CFD and LPT) was performed by Colli et al. (2015) by comparing numerical results against in-field measurements.

The drag coefficient is the crucial parameter controlling the particle behavior since it directly affects the hydrometeor fall velocity and its response after a change in wind speed. The OpenFOAM library contains several drag models, none of which is formulated for raindrops or snow crystals. A new model was added to the source code, with drag coefficient equations implemented for various ranges of the particle Reynolds number, as established a priori among those proposed in the literature by Folland (1988) and formulated starting from data published by Beard and Chuang (1987) and Khvorostyanov and Curry (2005). The model already adopted and validated in the work of Cauteruccio et al. (2021b) is here slightly improved by modifying the Reynolds number intervals

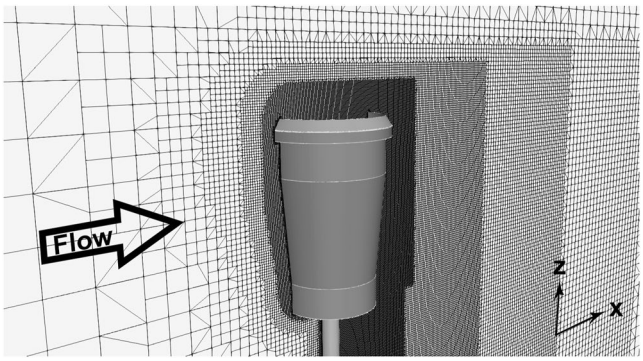

Figure 1. Sample section of the computational mesh along the longitudinal axis of the domain at $Y = 0$ for the CY-CAE instrument, showing the refinements created close to the instrument body. The black arrow indicates the wind direction.

(changing the threshold value from 400 to 320) to adjust the continuity of the drag function over the entire range.

2.1. Meshing and Airflow Simulation Setup

A numerical model of each investigated precipitation measuring instrument, including their supporting pole, was realized in the Standard Triangulation Language format. The computational mesh was produced within OpenFOAM v2012 (OpenFoam, 2020), for a 5 m long, 3 m wide, and 2.5 m high simulation domain. The longitudinal axis (X) of the computational mesh is set parallel to the wind direction, the vertical axis (Z) is directed upward, while the Y-axis is normal to the (X, Z) plane. The origin of the reference system is along the instrument symmetry axis and positioned at the height of the instrument collector. The mesh has a maximum cell size of 0.125 m and is progressively refined up to 2.5 mm near the instrument walls to reproduce the surface curvature and geometric details of the instrument body. An (X, Z) section of the computational mesh at $Y = 0$ is presented in Figure 1 for a sample instrument geometry (the CY-CAE).

Depending on the size of the instrument, the final mesh contains between three and 6 million cells and the values of typical mesh size and quality parameters, including the non-orthogonality, skewness, and aspect ratio, are listed in Table 2. These are used to identify highly distorted cells that could affect the solution and their values should be minimized. In Table 2, the quality parameters for all instruments are shown to be acceptable for external aerodynamic simulations (see e.g., Aqilah et al., 2018).

The aerodynamic behavior at undisturbed wind speed values (U_{ref}) equal to 2, 5, 10, 15, and 20 m s^{-1} was simulated for each instrument. This allows providing adjustment curves even in the case of intense events, typical of a tropical climatology or mountainous environment, where high wind speed may be present during precipitation (see e.g., Cauteruccio et al., 2023; Nitu et al., 2018).

2.2. Particle Tracking Setup

Since particle-to-particle interactions are neglected, hydrometeors are inserted in the domain along a regular grid, with variable extension and spacing depending on the gauge collector diameter. To ensure that all trajectories that potentially cross the collector area are simulated a rectangular grid is used, 2 diameters wide and 4.5 diameters long, while the grid spacing is about 1.5% of the diameter. The coordinates of the center of the rectangle and its vertical position (release height) are obtained by computing the fall distance and horizontal displacement of a single hydrometeor in undisturbed flow velocity conditions.

Liquid and solid precipitation are modeled by considering 11 equivolumetric particle diameters, equal to 0.25, 0.5, 0.75 mm and from 1 to 8 mm at 1 mm increments. We assume spherical particles with density, ρ (gr cm^{-3}), being expressed by a power law formulation as a function of the particle diameter, D (cm), (Rasmussen et al., 1999) in the form:

Table 2
Mesh Size and Quality Parameters Per Each Investigated Instrument

Instrument	No. cells	Max non-orthogonality (°)	Avg. non-orthogonality (°)	Max skewness (–)	Max aspect ratio (–)
CH-GEO	5,869,672	64.45	6.20	1.97	22.73
CH-OTT	5,607,023	64.53	6.64	3.99	18.04
CY-CAE	5,263,038	64.85	6.46	4.61	21.37
CY-LAM	2,858,560	64.38	6.31	3.38	18.42
IC-EML	3,438,901	64.63	6.37	3.45	20.48
SH-AES	5,835,018	63.70	6.99	3.19	20.80

Table 3
Parameters of the Power Law Dependency of the Hydrometeor Density on the Particle Size

3	α (gr cm^{-3})	β
Rain	1	0
Dry snow	0.017	−1

$$\rho(D) = \alpha \cdot D^{\beta} \quad (1)$$

where the values of the parameters are given in Table 3 for both liquid and solid particles (the characteristics of dry snow are used, due to its high sensitivity to aerodynamic effects).

Hydrometeors are inserted with an initial horizontal velocity component equal to the undisturbed flow velocity and a vertical velocity component equal to the particle terminal velocity (w_T). The terminal velocity is obtained once the gravitational force and the aerodynamic force (due to drag) are in equilibrium, meaning that the particle cannot accelerate further. To maintain consistency with the numerical model, the terminal velocity was computed by using the drag coefficient previously shown and derived from the work of Cauteruccio et al. (2021b).

3. Results

3.1. Computational Fluid Dynamics Results

Results are obtained in terms of the magnitude and components of the airflow velocity and of the turbulent kinetic energy over the entire simulation domain. In this section the main features affecting the hydrometeor trajectories are summarized in terms of maps and profiles of the normalized magnitude and vertical component of the airflow velocity (indicated with U_{mag}/U_{ref} and U_z/U_{ref}, respectively).

As a sample of the large numerical data set obtained, airflow velocity maps in the (X, Z) section of the flow field at $Y = 0$, for $U_{ref} = 5$ m s^{-1}, are presented in Figure 2 for the CH-OTT and IC-EML instruments (see Chinchella et al., 2023 for maps of all gauges). The red zones in the left-hand panels indicate a larger flow velocity than the undisturbed wind speed, therefore $U_{mag}/U_{ref} > 1$, while in the blue zones the flow velocity is lower than the undisturbed wind, and $U_{mag}/U_{ref} < 1$. Instead, the red zones in the right-hand panels indicate upward flow velocity components, with $U_z/U_{ref} > 0$, while downward components occur in the blue zones, where $U_z/U_{ref} < 0$.

The separation layer above the instrument collector between the accelerated airflow in the upper part (red zones, able to drag particles away from the collectors) and a recirculation zone in the lower part and inside of the collector (blue zones, contributing to catch particles) is the relevant feature observed in the map of the normalized velocity magnitude reported in Figure 2 (left-hand panels).

By analyzing the whole set of simulations, not reported here for the sake of conciseness, it appears that for the chimney-shaped gauges (CH-GEO and CH-OTT) the separation layer progressively detaches from the collector in the downstream direction. For the shielded and the inverted conical instruments (SH-AES and IC-EML) the

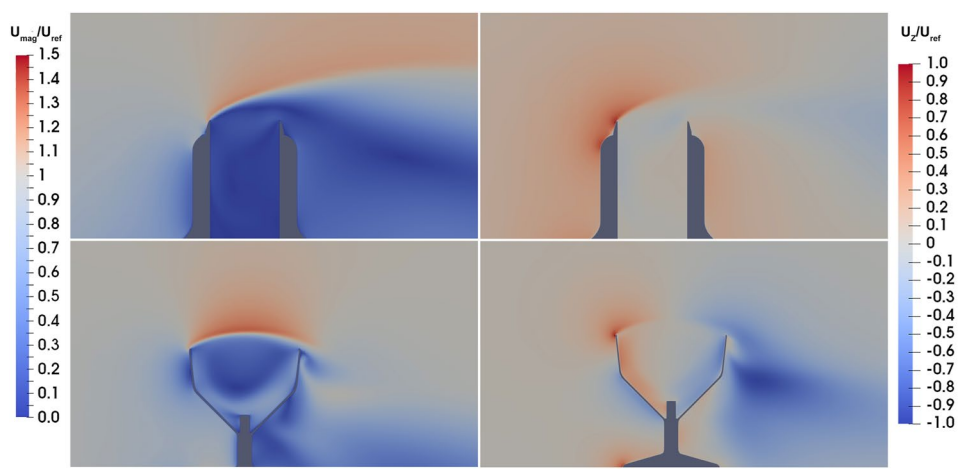

Figure 2. Sample airflow simulation for the CH-GEO (top panels) and IC-EML (bottom panels) instruments at $U_{ref} = 5$ m s^{-1}; maps of the normalized magnitude U_{mag}/U_{ref} and vertical component U_z/U_{ref} of the airflow velocity (left- and right-hand panels, respectively), along the (X, Z) section of the domain at $Y = 0$. The wind direction is from left to right.

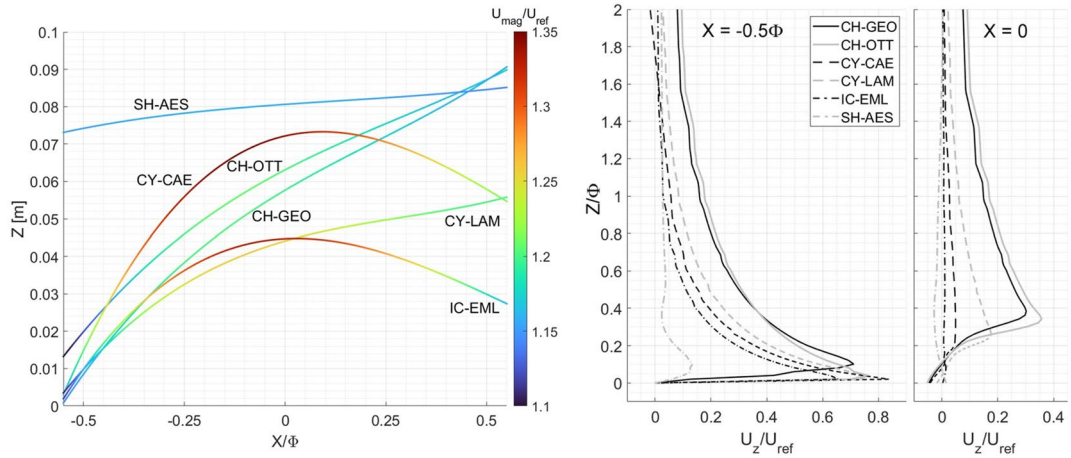

Figure 3. Longitudinal profiles of the position of the maximum non-dimensional airflow velocity U_{mag}/U_{ref}, color coded according to the associated numerical value (left) and vertical profiles of the non-dimensional vertical velocity U_z/U_{ref} over the collector of the investigated instruments (right), obtained from numerical simulation performed at $U_{ref} = 5$ m s^{-1}.

separation layer is quite closed over the downwind edge of the collector, foreshadowing a less relevant effect. The nearly cylindrical gauges (CY-CAE and CY- LAM) show an intermediate behavior.

The balancing of the updraft and downdraft airflow velocity components respectively occurring upstream and downstream of the center of the collector is the relevant feature of the maps of the normalized vertical velocity component since this affects the fall velocity of traveling particles. For the shielded and the inverted conical instruments (SH-AES and IC-EML) the two components are balanced, while the updraft component is largely prevalent above the collector of the chimney-shaped instruments (CH-GEO and CH-OTT), implying a stronger impact on particle trajectories. Again, nearly cylindrical gauges (CY-CAE and CY-LAM) have an intermediate behavior.

A synthetic representation of the aerodynamic behavior of the investigated instruments is presented and compared in Figure 3. In the left-hand panel, the longitudinal profile of the position of the maximum value of the normalized flow velocity magnitude (U_{mag}/U_{ref}) above the instrument collector is reported, color coded according to its numerical value. In the right-hand panel, the vertical profiles of the normalized vertical velocity (U_z/U_{ref}) at the upstream edge ($X/\Phi = -0.5$) and at the center ($X/\Phi = 0$) of the collector are reported.

It is evident from the graph in the left-hand panel that the entire profile for the shielded gauge (SH-AES) is far above the collector (always more than half a diameter) with very low values of the maximum velocity (always less than 15% above the U_{ref}), implying a limited impact on the hydrometeor trajectories. The two chimney-shaped instruments (CH-GEO and CH-OTT) also show relatively low maximum velocity patterns (about 20% higher than U_{ref}), but their profiles start at very low elevation and increase with the longitudinal coordinate while increasing the velocity as well, reaching a higher elevation at the downwind edge of the collector than all other instruments, yielding a strong deflection of the hydrometeor trajectories.

The inverted conical instrument (IC-EML) initially shows a similar pattern, but with a slightly larger velocity (about 30% higher than U_{ref}) in the central part of the profile and a lower elevation at the downstream edge, with an expected positive impact on the hydrometeor trajectories. The two cylindrical instruments are quite different from each other, with the CY-CAE showing the strongest velocity pattern (up to about 33% higher than U_{ref}), which spans for most part of the profile above the instrument collector, yielding a sustained effect on the falling hydrometeors. The maximum velocity profile for the CY-LAM mimics the one of the IC-EML above the first half of the collector, but with much lower velocity values (approximately 25% higher than U_{ref}), then rises to reach the same value of the CY-CAE at the downstream edge.

In the right-hand panel, the vertical profiles of the normalized vertical component of the airflow velocity show that the shielded gauge (SH-AES) has a very limited updraft at the collector's edge, which even reverse into a slight downdraft component at the center of the collector, appearing optimal in terms of catching performance. The two chimney-shaped gauges (CH-GEO and CH-OTT), indicated with solid black and gray lines, show very strong updraft components in both longitudinal sections, with significant values even at the center of the collector. This suggests a continued, sustained

uplift effect on the falling hydrometeors enhancing the diversion from their undisturbed trajectory. The inverted conical instrument (IC-EML) shows the least updraft at the edge of the collector after the SH-AES and a nearly null updraft at the center of the collector, foreshadowing a very limited impact on the hydrometeor trajectories. The two cylindrical instruments (CY-CAE and CY-LAM) show opposite behavior, with the CY-CAE having the strongest updraft among all instruments at the collector's edge, while the updraft at the center of the collector is larger for the CY-LAM, yielding an inconclusive assessment of the possible impact on the hydrometeor trajectories. Differences in the aerodynamic behavior of the two CY gauge is mainly ascribable to the protruding rim mounted on the CY-CAE. The role of the rim is confirmed by the difference in the aerodynamic behavior of the two CH gauges, since their geometries differ from each other mainly for the presence of a shaped rim in the CH-OTT.

3.2. Lagrangian Particle Tracking Model Results

As an example of the LPT results, two sets of trajectories for sample incoming hydrometeors of different equivolumetric diameter are presented in Figure 4 for liquid precipitation. The simulation was performed at $U_{ref} = 5$ m s^{-1} for two of the investigated instruments (the CY-CAE and the SH-AES). The changes in the vertical fall velocity (w) along the drop trajectories are highlighted by the color coding, which indicates the actual fall velocity per each position of the drop along its trajectory, normalized with the terminal velocity (w_T). When less than unity, the drop is slowed down by the flow updraft while negative values indicate upward velocity.

The trajectories of the larger drops (e.g., 2 mm—right panels) are nearly unaffected by the airflow features above the instrument collector, having a large terminal velocity, and the reduction of their fall velocity due to the updraft is very limited (normalized values are close to unity). Nearly all particles are suitably collected in this case yielding a negligible effect of the wind on the measured precipitation.

Small size drops (e.g., 0.25 mm—left panels) are instead strongly affected by the updraft and acceleration induced by the presence of the instrument immersed in the wind field and are subject to deviations and a dramatic reduction of their fall velocity well below the terminal value, with even opposite fall velocity (upward motion) in some portions of the domain above the instrument collector. In such conditions, the collection of hydrometeors is limited to a few trajectories that do enter the collector close to the downwind edge, and the impact of wind on precipitation measurements is the strongest.

The deflection of the trajectories of a sample particle (a single raindrop with diameter 0.25 mm) is shown in Figure 5 (upper panel) for an undisturbed wind velocity $U_{ref} = 5$ m s^{-1}. Comparison of the fate of a single drop

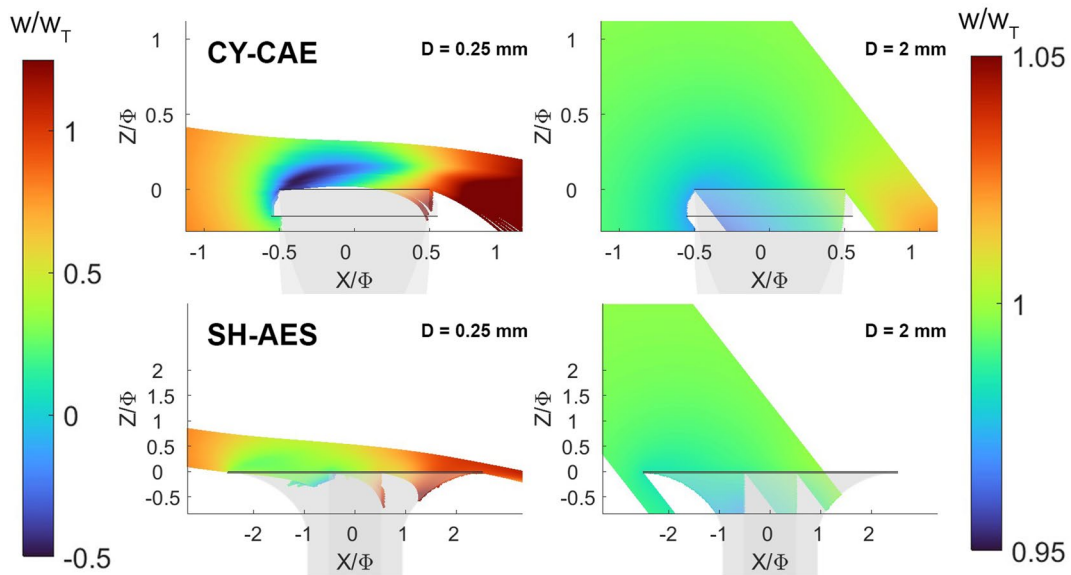

Figure 4. Raindrop trajectories along the longitudinal section of the domain at $Y = 0$, for two sample instruments (the CY-CAE and the SH-AES), at $U_{ref} = 5$ m s^{-1} and for two equivolumetric diameters, 0.25 mm (left panels) and 2 mm (right panels). The color coding reflects the fall velocity of the drop along each trajectory, normalized with the terminal velocity. Note that for the large size particles a narrower range was necessary for the color coding to highlight the limited wind effect.

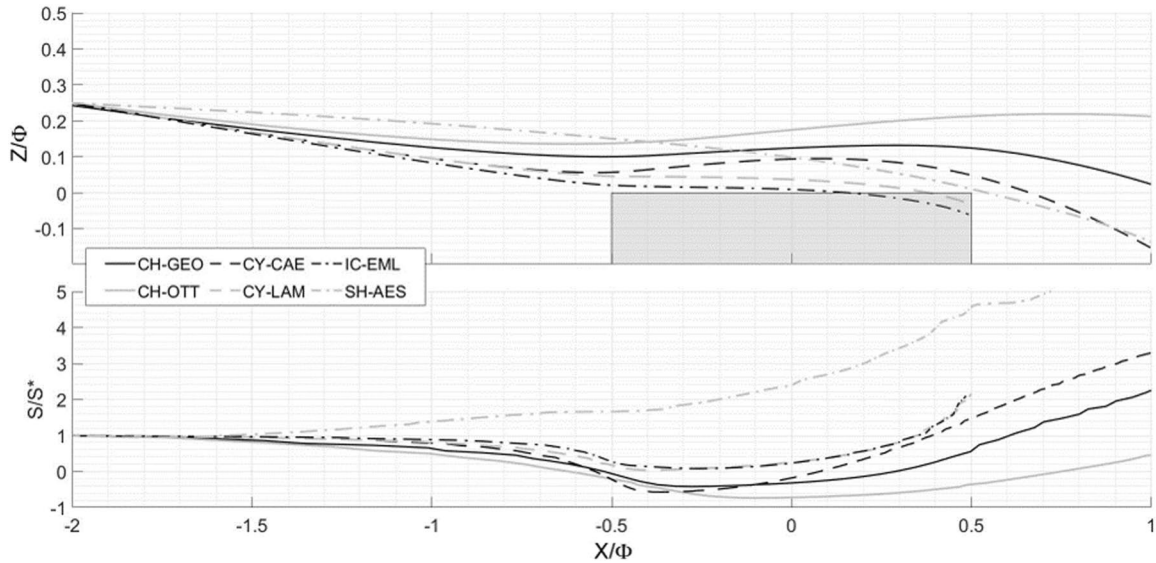

Figure 5. Trajectories of a water drop starting from the normalized fixed position ($X/\Phi = -2$, $Y/\Phi = 0$, and $Z/\Phi = 0.25$) within the airflow field induced by the investigated gauges (top panel) and local slope along each trajectory (bottom panel), normalized with the slope at the starting position.

starting from a fixed normalized position ($X/\Phi = -2$, $Y/\Phi = 0$, and $Z/\Phi = 0.25$) upstream of the collector within the disturbed airflow field produced by each investigated instrument is provided. The evolving slope of the trajectory $S = dZ/dX$, normalized with the slope at the starting position S^*, is also reported in the lower panel to better highlight the deviation from the undisturbed trajectory, which is expected to have $S/S^* = 1$.

In the top panel, the most deviated trajectories are those aiming at the collector of the two chimney-shaped instruments (CH-GEO and CH-OTT), with the CH-OTT underperforming all other instruments, while the less deviated is the one aiming at the aerodynamic instrument (IC-EML). The normalized slope (S/S^*) remains always positive only for the shielded gauge (SH-AES), meaning that the updraft effect on hydrometeor trajectories is minimized for that instrument. Note that, since normalized with the collector's diameter, the initial slope of the trajectories starting in the same normalized position is not the same for all instruments. The drop aiming at the IC-EML instrument is deviated very late along its trajectory, close to the collector, and only slightly. The two cylindrical instruments show a different behavior, with the CY-LAM experiencing a limited and late deviation, while the CY-CAE is significantly deviated similarly to the chimney-shaped instruments. Note, however, that the latter instrument has the largest collector's diameter, therefore the normalization adopted in the graph visualizes a reduced deviation than the chimney-shaped instruments, while the actual deviation is way larger.

For this reason, the bottom panel is also provided, where the normalized slope of each trajectory is reported. Values lower than unity indicate an upward deviation of the drop trajectory, meaning that significant updraft is reducing the fall velocity of the drop, while accelerated flow is increasing the longitudinal velocity. When the normalized slope reaches its minimum value and starts to increase, the drop trajectory is aiming downward by recovering the contribution of the gravity acceleration, which is less evidently counteracted by the airflow velocity components. All instruments show this effect, which starts very early for the SH-AES with normalized slope always larger than unity (because of the large size shield), while it is mostly evident above the downstream half of the collector for all other instruments. Note that the downward slope of the trajectory is recovered very late for the two chimney-shaped instruments (CH-GEO and CH-OTT) and mainly beyond the edge of the collector (too late to significantly contribute to collect the drop). The trajectory aiming at the CY-CAE has a similar behavior, with both an earlier upward deviation and an earlier downward deviation. The normalized slope curves for the IC-EML and the CY-LAM are very close to each other (about superimposed in the graph), reflecting very close performance.

3.3. Overall Catch Ratio

For each instrument geometry, given the size of the incoming hydrometeor, numerical simulation allows computing the catch ratio (CR) as a function of the wind speed. The CR is defined as the ratio between the number of

hydrometeors that are collected by the instrument under the effect of wind and the number of hydrometeors that would have been collected if the instrument was transparent to the wind. The CR is independent on the local climatic characteristics and is therefore representative of the aerodynamic behavior of the specific instrument geometry alone, with respect to individual hydrometeors.

Widening the interpretation of the instrument behavior from monodisperse to natural precipitation events, the formulation of the CR was expanded by Nešpor and Sevruk (1999) by taking the integral of the CR over the range of hydrometeor equivolumetric diameters. Since the number of hydrometeors in a precipitation event varies with size according to the PSD, taking such integral requires assuming a specific formulation for the PSD.

However mathematically defined, the PSD formulation was demonstrated to heavily depend on the PI (Colli et al., 2020). Precipitation intensity is indeed an integral variable obtained by taking the integral of the PSD, weighted with the particle fall velocity. Therefore, the relationship between the PSD and PI is inherent to their very same definition, and similar considerations hold for the terminal velocity of the falling hydrometeors, which is a well-known function of their size, density, and shape.

Details of this integral computation can be found in Colli et al. (2016b), where the numerical and volumetric collection efficiency are defined as the ratio of the integral of the PSD, weighted with the associated CR, over the undisturbed value (where a unity CR is used).

In this work, we obtained individual CR values per each numerical simulation performed at a given undisturbed wind speed and particle diameter, for both liquid and solid precipitation. In Figures 6 and 7, numerical CR values (symbols) are reported for drops and snowflakes of sample diameters. As expected, the investigated instruments show a similar behavior, where the CR values decrease with increasing the wind speed and decreasing the equivolumetric particle diameter (from circles to diamonds in the graphs). The rate of decrease depends on the instrument geometry but is also a function of the particle size, with the CR values of small size particles decreasing more abruptly than those of large size particles. This is due to the larger influence of wind on the small-size light particles, which tend to closely follow the streamlines and have their fall velocity affected by the aerodynamic behavior of the instrument.

For each gauge geometry, the numerical CR values were fitted with an exponential function (dashed lines in Figures 6 and 7) as:

$$CR(D,U) = \exp[-\lambda(D)\cdot U] \tag{2}$$

where λ expressed in $(\mathrm{m\ s^{-1}})^{-1}$ is the best-fit parameter. The values of λ are reported in Table 4, for both liquid and solid precipitation, together with the mean coefficient of determination per each tested geometry.

Table 4
Exponential Best-Fit Parameter, λ, of the Catch Ratio of Liquid and Solid Precipitation, for the Various Gauge Geometries and Equivolumetric Particle Diameters

		Equivolumetric particle diameter (mm)							
Instrument	Particle phase	0.25	0.5	0.75	1	2	4	8	R^2_{avrg}
CH-GEO	Liquid	0.4474	0.0428	0.0149	0.0080	0.0024	0.0008	0.0002	0.915
	Solid	0.2707	0.2751	0.3198	0.3158	0.2735	0.2429	0.2247	0.971
CH-OTT	Liquid	0.4174	0.0560	0.0180	0.0093	0.0027	0.0009	0.0003	0.969
	Solid	0.4174	0.3752	0.3768	0.3707	0.3294	0.2936	0.2716	0.964
CY-CAE	Liquid	0.5266	0.0514	0.0163	0.0082	0.0021	0.0006	0.0002	0.970
	Solid	0.5700	0.4055	0.3529	0.3273	0.2835	0.2565	0.2411	0.953
CY-LAM	Liquid	0.2885	0.0259	0.0097	0.0053	0.0017	0.0007	0.0003	0.951
	Solid	0.4424	0.3502	0.2962	0.2647	0.2035	0.1695	0.1506	0.987
IC-EML	Liquid	0.2603	0.0242	0.0085	0.0044	0.0011	0.0003	−0.0001	0.959
	Solid	0.4873	0.3316	0.2721	0.2467	0.1897	0.1597	0.1539	0.958
SH-AES	Liquid	0.1680	0.0240	0.0081	0.0042	0.0012	0.0005	0.0002	0.914
	Solid	0.2661	0.2031	0.1749	0.1582	0.1438	0.1302	0.1219	0.965

Note. The average coefficient of determination over all particle diameters is reported in the last column.

Table 5
Best-Fit Parameters for the Variation of the Exponent λ With the Particle Size (Liquid and Solid Precipitation) for the Investigated Instruments

Instrument	Particle phase	Best-fit parameters				Coefficient of determination $(1 - R^2)$
		c	k	m	n	
CH-GEO	Liquid	0.0329	0.0490	−7.8880	17.1673	7.84E−07
	Solid	0.3741	0.0395	0.3409	−0.0103	5.96E−03
CH-OTT	Liquid	0.0916	0.0158	−7.7242	18.5584	3.51E−06
	Solid	0.4240	0.0238	0.2337	−0.0096	2.52E−02
CY-CAE	Liquid	0.0345	0.0504	−7.6296	15.9486	5.43E−06
	Solid	1.6407	2.6587	12.3255	−0.0943	3.28E−03
CY-LAM	Liquid	0.0469	0.0547	−10.0965	27.7452	1.04E−06
	Solid	0.6691	0.3292	2.7931	−0.0229	9.44E−05
IC-EML	Liquid	0.0474	0.0118	−8.8349	22.4347	7.13E−06
	Solid	1.6042	1.6396	12.5392	−0.0857	7.03E−04
SH-AES	Liquid	0.0522	0.0118	−8.2305	22.1696	6.07E−06
	Solid	1.2854	3.4125	27.9711	0.0435	2.82E−03

To provide a continuous formulation of the exponential parameter λ as a function of the equivolumetric particle diameter D, an inverse second-order polynomial was fitted to the data in the form:

$$\lambda = \frac{(c + kD)}{(1 + mD + nD^2)} \tag{3}$$

where c,k,m and n are best-fit parameters. To justify the adoption of a three parameters function, the adopted fitting function (solid line) is compared with a power law (dashed line) in the log-log plot of Figure 8 (liquid precipitation) and Figure 9 (solid precipitation). The best-fit parameters for the variation of the exponent λ with the particle size, together with the associated complement of the coefficient of determination R^2, are reported in Table 5 for both liquid and solid precipitation.

In Figure 10, top panel, a comparison of the exponential parameter λ for liquid precipitation as a function of the drop diameter is provided for different instruments. As expected, the general tendency of λ for all gauges is to decrease with increasing the drop diameter. The obtained functional dependence shows that one instrument (the CH-OTT) has a strong decay of the CR with the wind velocity in the small size drop range and does recover a more uniform behavior when the drop size increases, while another one (the CY-LAM) has the opposite trend. However, the instruments visually cluster broadly in two groups, one with a generally stronger decay (larger values of λ) and a second one with a generally weaker decay (lower values of the parameter λ) at all drop size bins.

In the bottom panel of Figure 10, the same comparison is reported for solid precipitation. In this case, the two chimney-shaped instruments (CH-GEO and CH-OTT) maintain relatively high values of the parameter λ (implying a fast decrease of the CR with the wind velocity) at all particle diameters. The aerodynamic instrument (SH-AES), as expected, has the lowest values of the parameter λ (implying a slow decrease of the CR with the wind velocity) that slightly decreases with the particle size, while the steepest decrease of the exponential parameter λ is obtained for the IC-EML (aerodynamic) and the CY-LAM (cylindrical) instruments. The other cylindrical design (CY-CAE) has the worst behavior at small size particles among all the investigated instruments and is not able to recover much with increasing the particle size, remaining at levels that are typical of the chimney-shaped instruments even at the largest diameters.

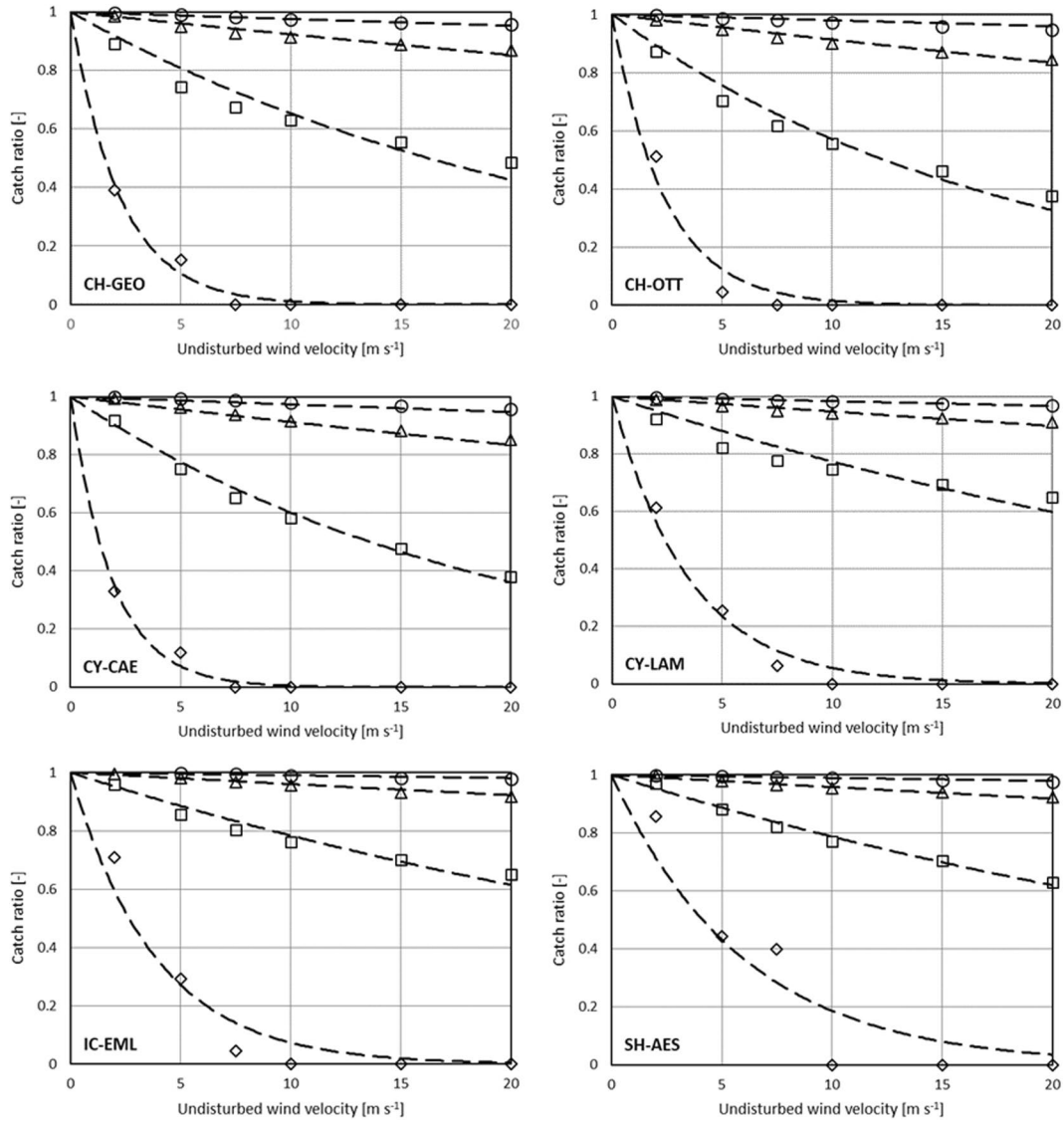

Figure 6. Catch ratio for sample selected drop diameters as a function of wind speed for the CH-GEO, CH-OTT, CY-CAE, CY-LAM, IC-EML, and SH-AES instruments. Symbols indicate numerical simulation results for $D = 0.25$ (diamonds), $D = 0.5$ (squares), $D = 1$ (triangles), and $D = 2$ mm (circles), while dashed lines represent the best-fit exponential functions per each sample diameter.

Per each particle size, the dependence of the CR on the wind velocity is a characteristic of the instrument geometry alone and makes no assumptions about the local wind and rainfall climatology at a specific measurement site. In this respect, the comparison of the CR functions is the most general representation of the result of the present work. To better highlight the consequences of choosing any given instrument geometry on the overall measurement bias (e.g., over the yearly precipitation amount), a specific particle size distribution and a local wind climatology must be assumed.

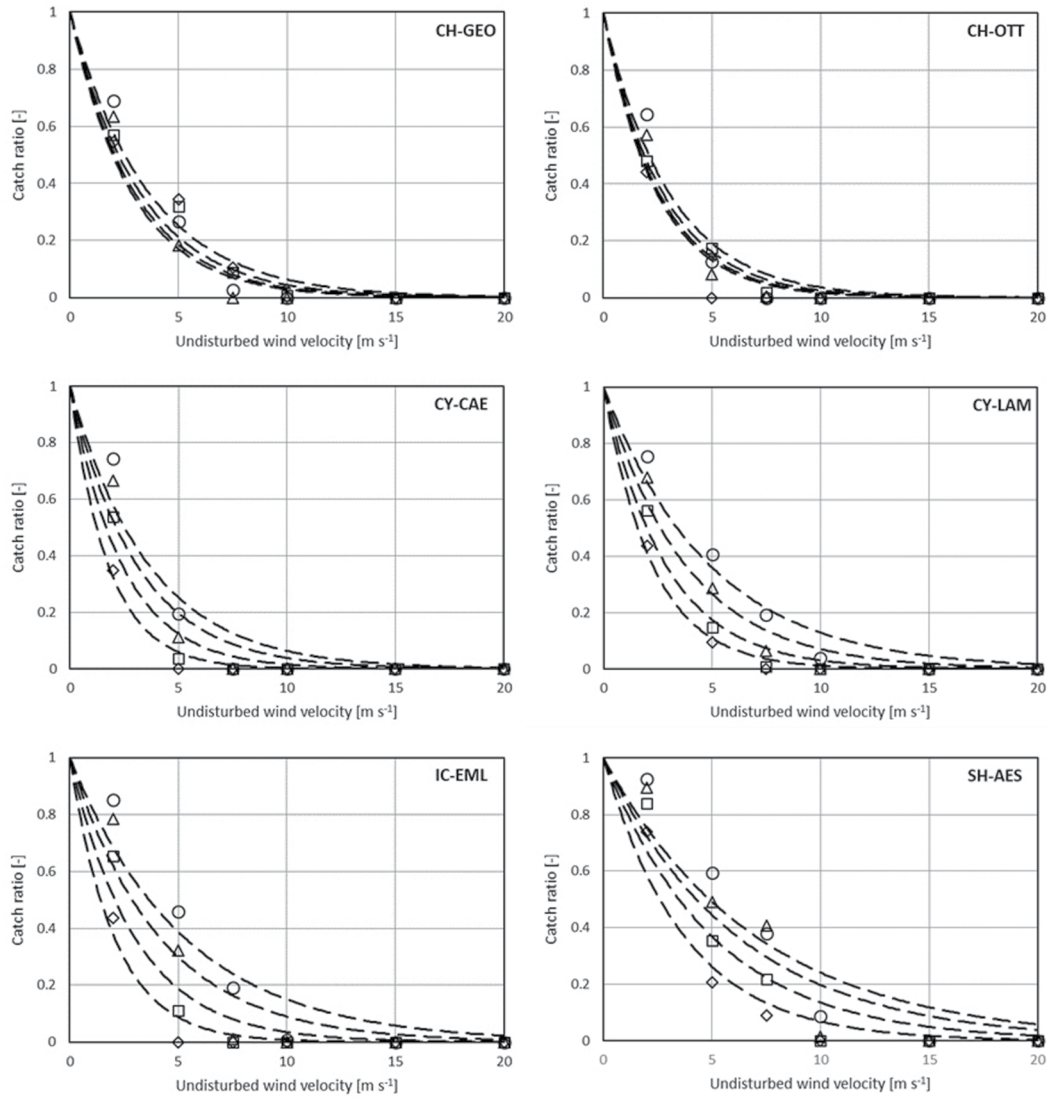

Figure 7. Catch ratio for sample selected snowflake diameters as a function of wind speed for the CH-GEO, CH-OTT, CY-CAE, CY-LAM, IC-EML, and SH-AES instruments. Symbols indicate numerical simulation results for $D = 0.25$ (diamonds), $D = 0.5$ (squares), $D = 1$ (triangles), and $D = 2$ mm (circles), while dashed lines represent the best-fit exponential functions per each sample diameter.

To avoid selecting any specific measurement site, a wind climatology with a uniform pdf is chosen, that is, with any wind velocity being observed with the same frequency at a virtual demonstrative site. As a representative variable for the behavior of a generic instrument, the Overall Catch Ratio (OCR) is introduced and calculated as the average CR obtained under a uniform wind climatology, as:

$$\mathrm{OCR}(D) = \frac{1}{U_{\max}} \int_{U=0}^{U_{\max}} CR(D, U)\, dU \tag{4}$$

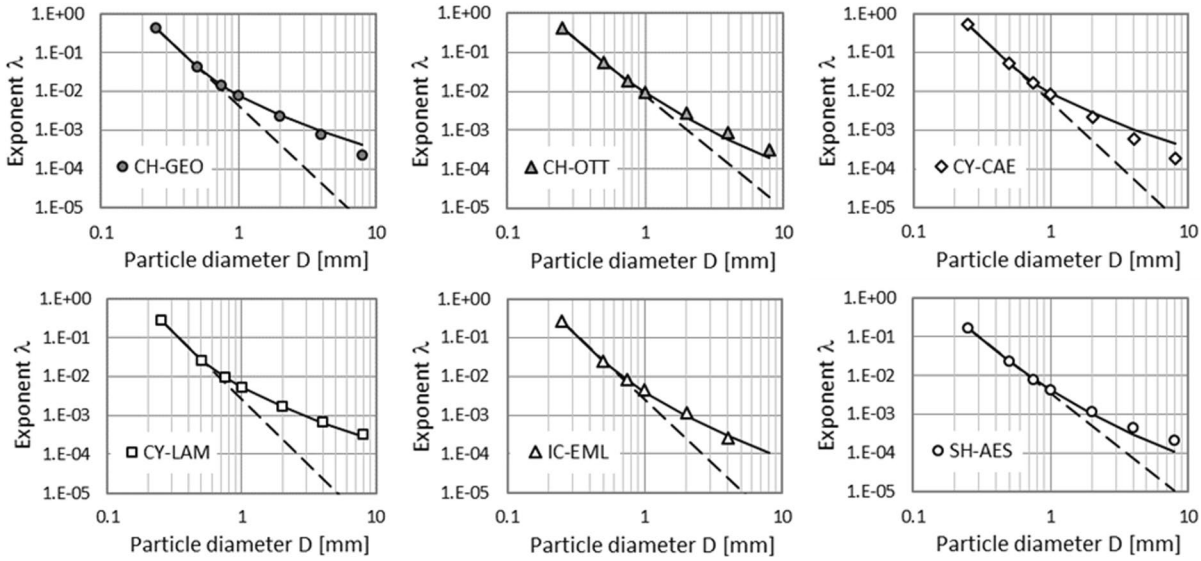

Figure 8. Decay with the drop size (liquid precipitation) of the exponential parameter λ of the catch ratio dependency on the wind speed for the investigated gauges. In each graph, symbols indicate numerical simulation results, the solid line is described by Equation 3, while the dashed line is the best-fit power law.

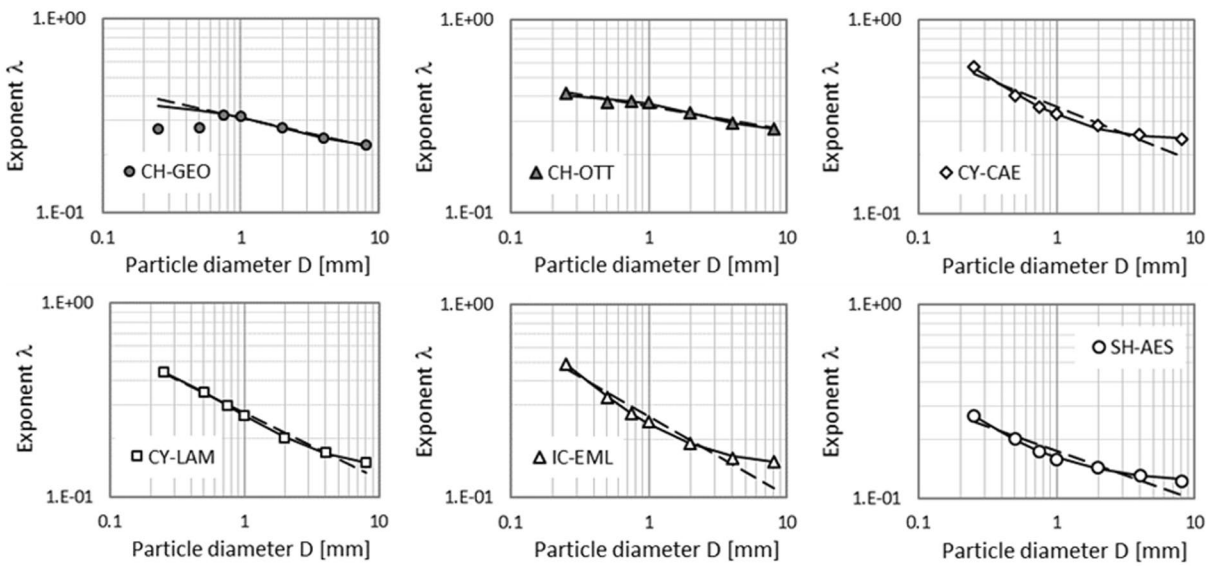

Figure 9. Decay with the particle size (solid precipitation) of the exponential parameter λ of the catch ratio dependency on the wind speed for the investigated gauges. In each graph, symbols indicate numerical simulation results, the solid line is described by Equation 3, while the dashed line is the best-fit power law.

10.1029/2023WR035098

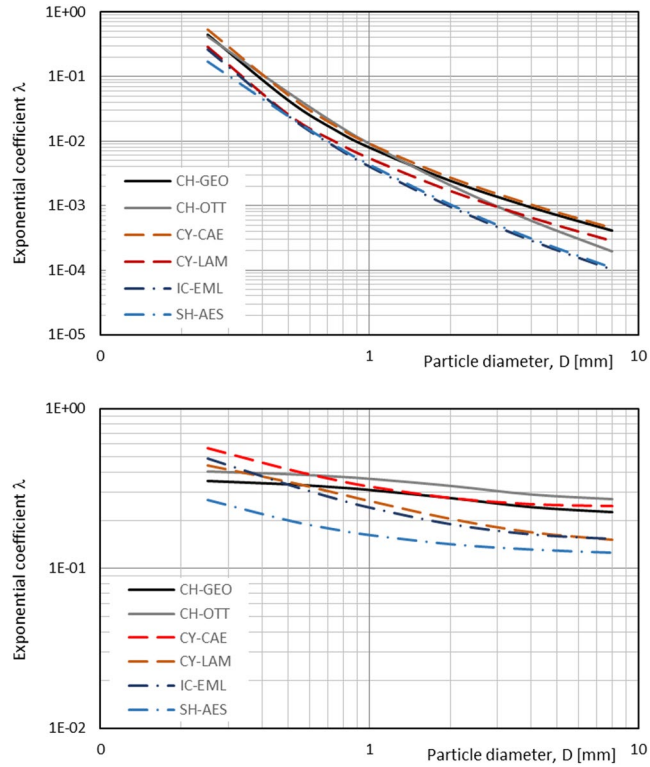

Figure 10. Comparison of the exponential parameter λ as a function of the particle size, for the six investigated gauges and for both liquid and solid precipitation in the top and bottom panel, respectively.

where D is the equivolumetric particle diameter and U the undisturbed wind velocity.

The OCR is obtained by taking the integral of the monodisperse CR over a range of wind speed values that is reasonably expected in natural conditions. This formulation assumes that the distribution of wind speed is uniform that is, every wind speed value is equally likely to occur. The assumption, although scarcely realistic at any specific measurement site, is proposed here to highlight the overall performance of each instrument, with some emphasis on the high wind speed range where the impact of the wind-induced bias is large. This is useful to compare the instrument aerodynamic behavior under the most demanding conditions.

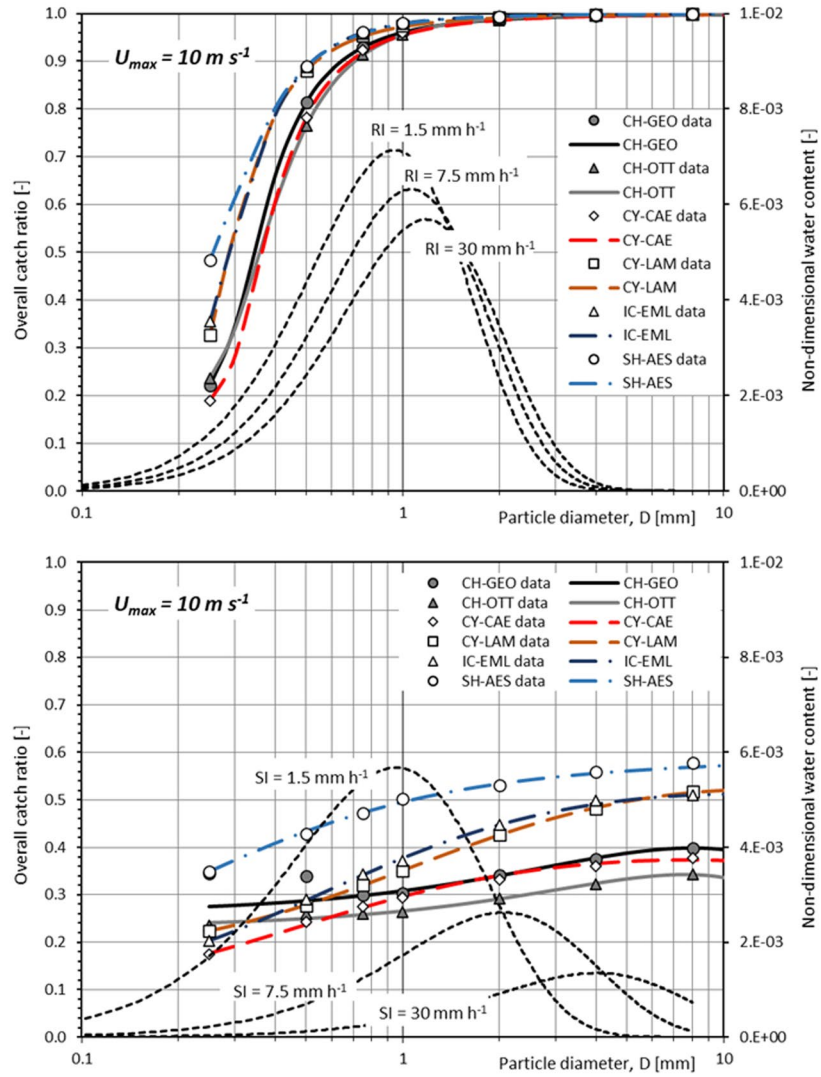

Figure 11. Overall Catch Ratio of the investigated instruments as a function of the particle size for liquid and solid precipitation, in the top and bottom panel, respectively, calculated under the hypothesis of wind climatology with uniform pdf and a maximum wind speed of 10 m s^{-1}. The non-dimensional water content (see Equations 6 and 7) is also shown with dotted lines for sample liquid (RI) and solid (SI) precipitation intensity events, based on the particle size distribution formulation shown in Equations A2–A4.

Using the derived exponential expression for the dependency of the CR on the wind velocity, the OCR becomes:

$$\mathrm{OCR}(D) = \frac{1}{U_{\max}} \int_{U=0}^{U_{\max}} e^{-\lambda(D)U}\, dU = \frac{1}{U_{\max}} \frac{1}{\lambda(D)} \left(1 - e^{-\lambda(D)U_{\max}}\right) \tag{5}$$

An example of the resulting OCR as a function of the particle size for both liquid and solid precipitation is shown and compared for all the investigated instruments in Figure 11. A wind climatology with uniform pdf is assumed with a maximum wind speed equal to 10 m s^{-1}. To help interpreting the impact of the instrument performance on precipitation measurements, the Liquid Water Content (LWC, see appendix) of precipitation events having different intensity between 1.5 and 30 mm hr^{-1} is also reported in the graphs.

The non-dimensional water content is obtained as the ratio between the LWC (Equations A5 and A6 in the Appendix for liquid and solid precipitation, respectively) and its integral (WC) over the whole range of diameters (Equations A9 and A15 in the Appendix for liquid and solid precipitation, respectively):

$$\mathrm{NWC}_L(D,\mathrm{RI}) = \frac{\mathrm{LWC}_L(D,\mathrm{RI})}{\mathrm{WC}_L} = \frac{\frac{\pi}{6}\cdot 10^{-6}\cdot N_0(\mathrm{RI})\cdot D^3\cdot \exp\left(-\lambda_0(\mathrm{RI})D\right)\cdot dD}{\frac{\pi N_0}{\lambda_0^4 10^6}} = \lambda_0^4\frac{D^3}{6}\exp\left(-\lambda_0(\mathrm{RI})D\right)\cdot dD \tag{6}$$

For solid precipitation:

$$| = \frac{0.017\cdot\frac{\pi}{6}\cdot 10^{-5}\cdot N_0(\mathrm{SI})\cdot D^2\cdot \exp\left(-\lambda_0(\mathrm{SI})D\right)\cdot dD}{\frac{0.017\pi N_0}{3\lambda_0^3 10^5}} = \lambda_0^3\frac{D^2}{2}\exp\left(-\lambda_0(\mathrm{RI})D\right)\cdot dD \tag{7}$$

For liquid precipitation, all instruments show a reduced OCR (below 80%) at the lower range of equivolumetric drop diameters ($D < 0.4$ mm), while all of them have very high OCR (above 95%) for $D > 1$ mm. The Percentage Mass Fraction (PMF) of raindrops having $D < 0.4$ mm is however limited, corresponding to about 5% of the total water volume at low PI—see Figure A1 in the Appendix. Instead, raindrops with $D > 1$ mm account for the most part of the rainfall volume, between 60% and 75% at precipitation intensities from 1.5 to 30 mm hr^{-1}. Therefore, the range where all instruments experience limited OCRs due to the wind is the less relevant portion of the PSD at any Rainfall Intensity (RI) level.

On the contrary, for solid precipitation, all instruments show OCR values below 60% over the whole range of investigated snowflake diameters. Below 1 mm, the OCR is always lower than 50%, although one instrument (the Nipher shielded one) performs much better than the others. At the same time, the PMF of solid precipitation is more smoothed and, although shifted toward large size particles, even at PI levels that are comparable to those of the above rainfall events and to natural events as well, is associated with much lower values of the OCR.

Differently from the case of liquid precipitation, where the ranking of instruments remains similar, with three of them (SH-AES, IC-EML and CY-LAM) being quite better than all others throughout the whole range of particle size bins, for solid precipitation the chimney-shaped instruments (the CH-GEO and the CH-OTT) are quite good at catching small size particles while their performance does not increase much with large size particles. Some instruments (the CY-LAM and the IC-EML) span from low performance at the small size particle range to high performance with large size particles. The SH-AES and the CY-CAE have similar trends with the particle diameter over the whole range but ranking among the best and worst performing instruments, respectively.

3.4. Overall Collection Efficiency

The Collected Water Content (CWC), as a function of the particle size, measured by the gauge when exposed to the wind is obtained as the LWC weighted with the OCR as follows:

$$\mathrm{CWC}(D,\mathrm{PI}) = V(D)\cdot\rho(D)\cdot N(D,\mathrm{PI})\cdot \mathrm{OCR}(D)\cdot dD \tag{8}$$

The CWC represents the volume fraction of water effectively reaching the gauge—under the effect of wind—and is compared with the actual volume fraction of precipitation (the LWC, computed in appendix in Equations A5 and A6) in Figure 12 for liquid and solid precipitation and for a sample gauge (the CY-CAE), as a function of the particle diameter and for selected values of the PI. Continuous and dashed lines represent the collected and actual WC, respectively. Very small particles—even if largely abundant in precipitation events—provide a limited contribution to the total volume. Large particles, though having a much larger volume individually, are quite rare and therefore account for a limited fraction of the total precipitation volume. Underestimation of the LWC is limited to particle diameters lower than about 2 mm in case of liquid precipitation, while for solid precipitation

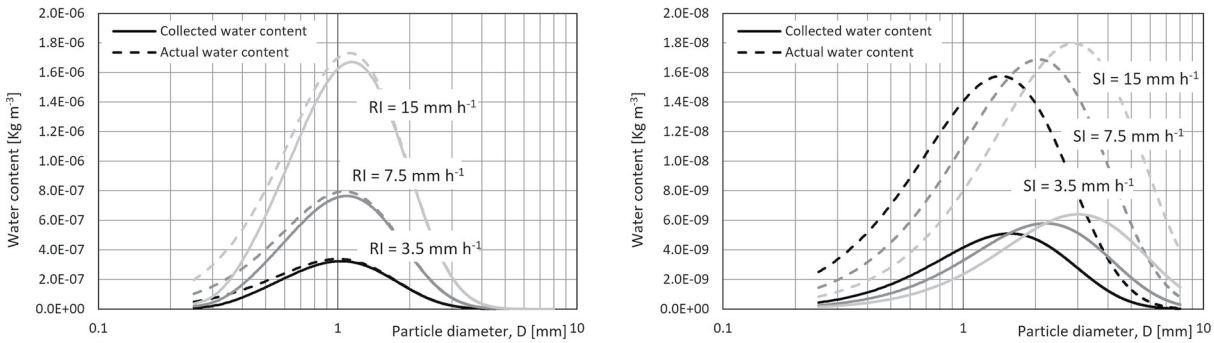

Figure 12. Comparison between the collected and actual water content with the particle size for a sample instrument (the CY-CAE) in case of liquid (left-hand panel) and solid (right-hand panel) precipitation of various intensity.

the underestimation is experienced throughout the entire particle diameter range, since snowflake trajectories are much more sensitive to the wind.

To compare the expected performance in the field for the six investigated CGs, the Overall Collection Efficiency (OCE) is here defined as:

$$\begin{aligned}\mathrm{OCE(PI)} &= \frac{1}{\mathrm{OCE_{max}(PI)}}\int_{D=D_{\min}}^{D_{\max}} \mathrm{CWC}(D)dD \\ &= \frac{1}{\mathrm{OCE_{max}(PI)}}\int_{D=D_{\min}}^{D_{\max}} V(D)\cdot\rho(D)\cdot N(D)\cdot \mathrm{OCR}(D)dD\end{aligned} \tag{9}$$

where the maximum of the OCE is obtained for an OCR equal to unity for each particle size, wind speed and PI. Considering the exponential formulation of the PSD and the definition of OCR, the OCE can be written as:

$$\begin{aligned}\mathrm{OCE(PI)} = \frac{1}{\mathrm{OCE_{max}(PI)}}\int_{D=D_{\min}}^{D_{\max}} &\pi\frac{D^3}{6}\cdot\frac{\alpha}{10^6}\left(\frac{D}{10}\right)^{\beta} \\ &\cdot N_0(\mathrm{PI})\exp[-\lambda_0(\mathrm{PI})D]\cdot\frac{1}{U_{\max}}\frac{1}{\lambda}\left(1-e^{-\lambda U_{\max}}\right)dD\end{aligned} \tag{10}$$

where α and β are listed in Table 3. By substituting the dependency of λ on D, as in Equation 3, the OCE becomes:

$$\begin{aligned}\mathrm{OCE(PI)} = \frac{1}{\mathrm{OCE_{max}(PI)}}\frac{\pi}{6}\frac{\alpha}{10^6}N_0(\mathrm{PI})\frac{1}{U_{\max}}\int_{D=D_{\min}}^{D_{\max}} &D^{3+\beta}\cdot\exp[-\lambda_0(\mathrm{PI})D] \\ \cdot\frac{1+mD+nD^2}{c+kD}&\left(1-e^{-\frac{(c+kD)}{(1+mD+nD^2)}\cdot U_{\max}}\right)dD\end{aligned} \tag{11}$$

The $\mathrm{OCE_{max}(PI)}$ computed for $\mathrm{OCR}(D)=1$, is:

$$\mathrm{OCE_{max}(PI)} = \frac{\pi}{6}\frac{\alpha}{10^6}N_0(\mathrm{PI})\int_{D=D_{\min}}^{D_{\max}} D^{3+\beta}\cdot\exp[-\lambda_0(\mathrm{PI})D]dD \tag{12}$$

Therefore, after substituting this equation in Equation 11, the OCE can be written as:

$$\mathrm{OCE(PI)} = \frac{\int_{D=D_{\min}}^{D_{\max}} D^{3+\beta}\cdot\exp[-\lambda_0(\mathrm{PI})D]\cdot\frac{1+mD+nD^2}{c+kD}\left(1-e^{-\frac{(c+kD)}{(1+mD+nD^2)}U_{\max}}\right)dD}{U_{\max}\int_{D=D_{\min}}^{D_{\max}} D^{3+\beta}\cdot\exp[-\lambda_0(\mathrm{PI})D]dD} \tag{13}$$

The OCE values computed by using Equation 13 therefore provide the expected performance of the gauge in the case of uniform wind climatology, as a function of the PI.

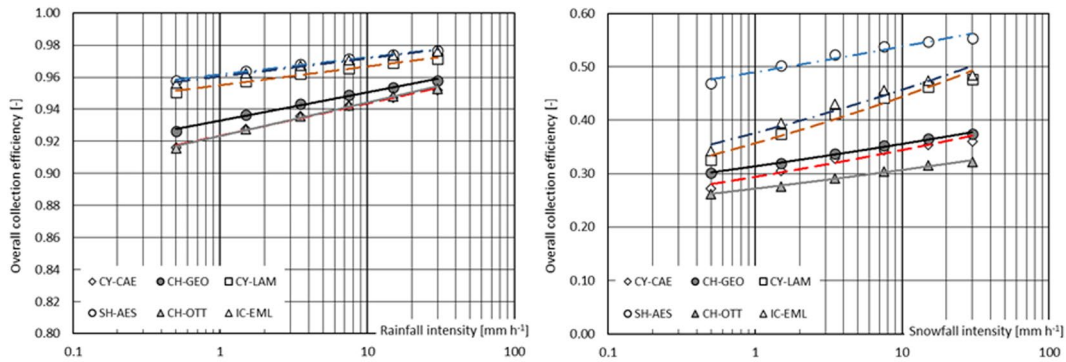

Figure 13. Calculated Overall Collection Efficiency values (symbols) as a function of precipitation intensity for the investigated instruments for (left-hand panel) liquid and (right-hand panel) solid precipitation, under the hypothesis of uniform wind climatology with a maximum wind speed of 10 m s^{-1}, based on the particle size distribution formulation shown in Equations A2–A4.

Figure 13 shows the OCE of the different CGs considered in this work for both liquid and solid precipitation. Like in the case of the OCR, the CY-CAE, CH-GEO, and CH-OTT instruments show lower performance than the other gauges in the measurement of liquid precipitation, with the CH-GEO performing slightly better. Meanwhile the SH-AES instrument is the best performing one, for the whole range of PI considered, closely followed by the other aerodynamic gauge, the IC-EML. The CY-LAM instrument slightly underperforms the two aerodynamic gauges but is significantly better than instruments belonging to the first group.

For solid precipitation, the SH-AES shielded instrument outperforms all other gauges by a wide margin, while the chimney-shaped instruments (CH-GEO and CH-OTT) are the worst performing ones, together with the CY-CAE, over the whole range of Snowfall Intensity (SI). Two instruments, the IC-EML and the CY-LAM show a different behavior with low performance at low precipitation rates but increasing their performance with increasing PI. This highlights the fact that proper aerodynamic design of both the outer shape of the gauge body (inverted conical for the IC-EML gauge) and the collector's rim (for the cylindrical CY-LAM) does result in superior performance under any PI event than in case of chimney-shaped or other cylindrical instruments.

Overall, instruments cluster in two distinct groups with chimney-shaped (CH-GEO and CH-OTT) and one cylindrical gauge (CY-CAE) underperforming at all PI events, while the aerodynamic gauge (IC-EML) and especially the shielded one (SH-AES) are by far the best performing instruments. One cylindrical gauge (CY-LAM) is just slightly below the two best performing instruments for both liquid and solid precipitation measurements.

Table 6
Power Law Best-Fit Parameters for the Dependency of Overall Collection Efficiency on the Liquid and Solid Precipitation Intensity for the Investigated Instruments

Instrument	Particle phase	Best-fit parameters		Coefficient of determination R^2
		q	r	
CH-GEO	Liquid	0.885	0.014	0.994
	Solid	0.165	0.065	0.994
CH-OTT	Liquid	0.870	0.016	0.994
	Solid	0.140	0.060	0.994
CY-CAE	Liquid	0.871	0.015	0.994
	Solid	0.154	0.076	0.994
CY-LAM	Liquid	0.919	0.009	0.994
	Solid	0.196	0.116	0.994
IC-EML	Liquid	0.930	0.009	0.993
	Solid	0.210	0.103	0.993
SH-AES	Liquid	0.931	0.009	0.994
	Solid	0.295	0.057	0.994

The OCE values as a function of PI can be fitted using a power law as:

$$\mathrm{OCE}(\mathrm{PI}) = q \cdot \mathrm{PI}^{r} \tag{14}$$

where q and r are the best-fit parameters, whose values are shown, for each investigated gauge, in Table 6.

4. Conclusions

Depending on their outer geometry, catching type instruments perform quite differently from each other in measuring precipitation under the presence of wind because of their aerodynamic behavior. Quantification of the wind-induced bias is provided in this work for five unshielded and one shielded gauge geometries in the form of the resulting catch ratios, for various equivolumetric particle diameters, as a function of the undisturbed wind speed. The impact on precipitation measurements therefore varies according to the local environmental conditions, including the wind speed during precipitation and the PI (which characterizes the PSD).

We introduce two synthetic overall measures of the instrument performance (OCR and OCE) to make such performance comparable over a range of possible environmental conditions. The OCR assumes a virtual site with uniform wind climatology, while the OCE requires assuming also the relationship between PI and the PSD.

The comparison led to the conclusion that the chimney-shaped instruments are the least suitable to measure precipitation (especially snow) in a windy environment, since they largely underestimate precipitation amount even in the case of high PI.

The instruments having less impact on the hydrometeor trajectories are the Nipher shielded one (especially for snow measurements) and the IC-EML (with the same OCE in case of rainfall). The inverted conical shape used in both cases is largely the most effective in reducing the bluff-body aerodynamic behavior.

The investigated cylindrical instruments have an intermediate behavior in terms of their bluff-body impact on the airflow but show very different performance due to their specific design. The CY-LAM is the best performing cylindrical instrument, though slightly less efficient than the inverted conical ones.

For instruments having the same outer geometry, a relevant role is ascribable to the shaping of the collector's rim. Indeed, the worst performant chimney-shaped instrument is the CH-OTT, having an abrupt change of its axial symmetric profile close to the top section with a resulting stronger updraft than the CH-GEO above the collector. Also, despite the quasi-cylindrical geometry, the presence of a protruding rim strongly affects the performance of the CY-CAE with respect to the CY-LAM, lowering them to the level of the two chimney-shaped instruments. The best performing instruments, the IC-EML, CY-LAM and SH-AES, have no abrupt geometrical variations close to their collector, thus limiting their bluff-body aerodynamic impact above the collector.

The results of this work can be exploited by operational users to select the most suitable outer geometry for instruments to be installed at sites with frequent wind. This would help managers of hydro-meteorological monitoring networks to minimize the impact of the wind-induced bias on the measurement accuracy and therefore improve the overall quality of the collected precipitation data sets. Furthermore, even if the presented correction curves cannot be used, performance ranking would still hold true in case any wind shield is added to the instrument. Indeed, the aerodynamic advantage of the gauge shape remains valid even under the reduced wind speed warranted by the wind shield.

For instruments that are already installed in sites with frequent windy conditions, this work provides the basic information needed to apply adjustments to the measured data. Indeed, provided a relationship between the parameters of the PSD and PI is available, the CR values reported above for six commonly employed precipitation measuring instruments allow the CE for the given site to be calculated and therefore the adjusted precipitation measurements (either in real time or a posteriori) to be obtained.

This work would finally help manufacturers of precipitation measuring instruments in that it provides hints about the best performing design solutions for aerodynamically efficient instruments. It also supports them in the possible upgrading of instruments with the existing design by introducing on-board adjustments of the measured precipitation that only require contemporary measurement of the wind velocity (often included in typical meteorological stations).

Appendix A

In this section the main variables used in the text are derived. Some further images are provided for clarification. Acronyms used throughout the paper are also listed.

The LWC (kg m^{-3}) is defined as the specific water mass associated with hydrometeors of diameter D (mm), and is calculated as:

$$\mathrm{LWC}(D) = \rho(D)V(D)N(D)dD \tag{A1}$$

where $\rho(D)$ is the density (kg m^{-3}), $V(D)$ the volume (m^3), and $N(D)$ the numerosity (m^{-3} mm^{-1}) of the particles having an equivolumetric diameter equal to D.

The number of hydrometeors per each size bin is given by the PSD equation, here formulated according to the exponential form proposed by Marshall and Palmer (1948) as:

$$N(D) = N_0 \cdot \exp(-\lambda_0 D) \tag{A2}$$

with the scale parameter N_0 and the shape parameter λ_0 being derived from literature results as a function of Precipitation Intensity (PI), expressed in mm h^{-1}, using a power law dependency in the form:

$$N_0(\mathrm{PI}) = a_{N_0} \cdot \mathrm{PI}^{b_{N_0}} \tag{A3}$$

$$\lambda_0(\mathrm{PI}) = a_{\lambda_0} \cdot \mathrm{PI}^{b_{\lambda_0}} \tag{A4}$$

For liquid precipitation we assume ($a_{N_0} = 835.910$ and $b_{N_0} = 0.894$) and ($a_{\lambda_0} = 3.286$ and $b_{\lambda_0} = -0.076$), as obtained by Cauteruccio and Lanza (2020) based on disdrometer data measured by Caracciolo et al. (2008). For solid precipitation, we assume ($a_{N_0} = 3800$ and $b_{N_0} = -0.870$) and ($a_{\lambda_0} = 2.550$ and $b_{\lambda_0} = -0.480$), as proposed by Gunn and Marshall (1958) and already exploited in assessing the wind-induced bias of solid precipitation measurements for example, by Cauteruccio, Chinchella, et al. (2021).

Based on the above microphysical characterization of the hydrometeors, the LWC assumes the following simple forms for liquid (LWC_L) and solid (LWC_S) precipitation:

$$\mathrm{LWC}_L(D, \mathrm{RI}) = \frac{\pi}{6} \cdot 10^{-6} \cdot N_0(\mathrm{RI}) \cdot D^3 \cdot \exp\left(-\lambda_0(\mathrm{RI})D\right) \cdot dD \tag{A5}$$

$$\mathrm{LWC}_S(D, \mathrm{SI}) = 0.017 \cdot \frac{\pi}{6} \cdot 10^{-5} \cdot N_0(\mathrm{SI}) \cdot D^2 \cdot \exp\left(-\lambda_0(\mathrm{SI})D\right) \cdot dD \tag{A6}$$

as a function of the hydrometeor diameter (D) and of the Rainfall Intensity (RI), and the Snowfall Intensity (SI), respectively.

The mass fraction of precipitation is here defined as the ratio of the integral Water Content (WC) contributed by hydrometeors having equal or lower size than a specified equivolumetric diameter over the total WC, in the form:

$$\mathrm{MF}(D) = \frac{\mathrm{WC}(D)}{\mathrm{WC}} = \frac{\int_0^D \mathrm{LWC}(\mathcal{D})d\mathcal{D}}{\int_0^\infty \mathrm{LWC}(\mathcal{D})d\mathcal{D}} = \frac{\int_0^D \rho(\mathcal{D})V(\mathcal{D})N(\mathcal{D})d\mathcal{D}}{\int_0^\infty \rho(\mathcal{D})V(\mathcal{D})N(\mathcal{D})d\mathcal{D}} \tag{A7}$$

For liquid precipitation, assuming the appropriate values of the coefficient α and β as reported in Table 4, solving the defined integral at the numerator results in:

$$\begin{aligned}\mathrm{WC}_L(D) &= \frac{\pi N_0}{6 \cdot 10^6}\left|\frac{1}{\lambda_0}\exp(-\lambda_0\mathcal{D})\left(-\mathcal{D}^3 + 3\left(-\frac{\mathcal{D}^2}{\lambda_0} - \frac{2\mathcal{D}}{\lambda_0^2} - \frac{2}{\lambda_0^3}\right)\right)\right|_0^D \\ &= \frac{\pi N_0}{\lambda_0^4 10^6}\left[1 - \frac{1}{6}\exp(-\lambda_0 D)\left(\lambda_0^3 D^3 + 3\lambda_0^2 D^2 + 6\lambda_0 D + 6\right)\right]\end{aligned} \tag{A8}$$

while computing the analogously defined integral at the denominator (the total WC) provide:

$$\mathrm{WC}_L = \frac{\pi N_0}{6 \cdot 10^6}\left|\frac{1}{\lambda_0}\exp(-\lambda_0\mathcal{D})\left(-\mathcal{D}^3 + 3\left(-\frac{\mathcal{D}^2}{\lambda_0} - \frac{2\mathcal{D}}{\lambda_0^2} - \frac{2}{\lambda_0^3}\right)\right)\right|_0^\infty = \frac{\pi N_0}{\lambda_0^4 10^6} \tag{A9}$$

since when D tends to infinity:

$$\lim_{D\to\infty} \exp(-\lambda_0 D)\left(\lambda_0^3 D^3 + 3\lambda_0^2 D^2 + 6\lambda_0 D + 6\right) = 0 \tag{A10}$$

Therefore, the mass fraction for liquid precipitation is easily obtained analytically as:

$$\mathrm{MF}_L(D) = 1 - \frac{1}{6}\exp(-\lambda_0 D)\left(\lambda_0^3 D^3 + 3\lambda_0^2 D^2 + 6\lambda_0 D + 6\right) \tag{A11}$$

where λ_0 is a function of the rainfall intensity RI, as defined in Equation A4.

The Percentage Mass Fraction $\mathrm{PMF}_L(D)$ is plotted in Figure A1 (left-hand panel) over the range of equivolumetric diameters investigated in this work for different RI values, assuming $\lambda_0 = \lambda_0(\mathrm{RI})$ as obtained by Cauteruccio and Lanza (2020) based on disdrometric data measured by Caracciolo et al. (2008).

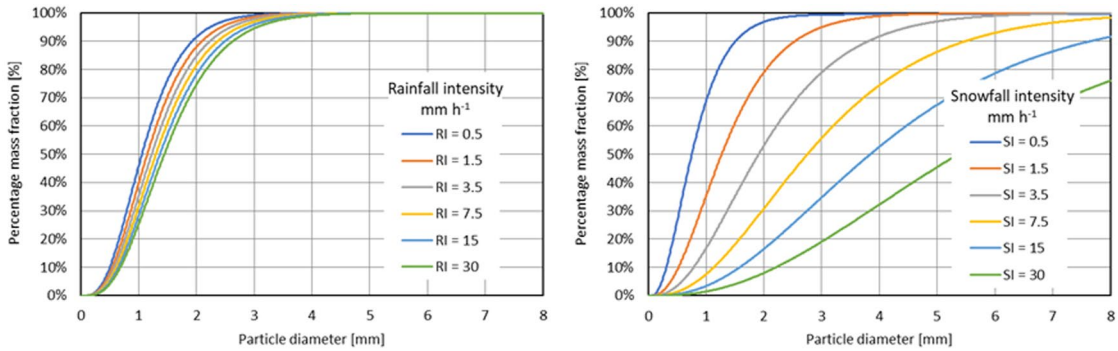

Figure A1. Percentage Mass Fraction of hydrometeors with the particle size, PMF(D), for liquid (left-hand panel) and solid (right-hand panel) precipitation at different precipitation intensity. Calculation is performed using the particle size distribution formulation shown in Equations A2–A4.

The PMF_L is instead plotted as a function of the rainfall intensity RI in Figure A2 (left-hand panel) for a few sample drop diameters. Note that, in this latter case, the dependency of PMF_L on RI can be suitably approximated by a simple power law to less than 0.6% over the whole range of RI from 0.1 to 30 mm hr^{-1}, in the form:

$$\mathrm{PMF}_L(\mathrm{RI}) \cong p(D) \cdot \mathrm{RI}^{g(D)} \tag{A12}$$

with the coefficient p and exponent g being expressed as a function of the equivolumetric drop diameter through a logarithmic and linear function, respectively.

The best-fit form of the PMF_L (with R^2 always larger than 0.98) is as follows:

$$\mathrm{PMF}_L \cong (0.5928 \ln(D) + 0.4723) \cdot \mathrm{RI}^{(0.112D - 0.268)} \tag{A13}$$

which can be used in practical calculations, provided the exponential PSD with the parameters obtained by Cauteruccio and Lanza (2020) based on disdrometer data measured by Caracciolo et al. (2008) is deemed acceptable for the site of concern.

For solid precipitation, assuming the appropriate values of the coefficient α and β as reported in Table 3, the defined integral at the numerator is instead calculated as:

$$\begin{aligned} \mathrm{WC}_S(D) &= \frac{0.017\pi N_0}{6 \cdot 10^5} \left| \exp(-\lambda_0 D) \left(-\frac{D^2}{\lambda_0} - \frac{2D}{\lambda_0^2} - \frac{2}{\lambda_0^3} \right) \right|_0^D \\ &= \frac{0.017\,\pi\,N_0}{6\,\lambda_0^3\,10^5} \left[2 - \exp(-\lambda_0 D) \left(\lambda_0^2 D^2 + 2\lambda_0 D + 2 \right) \right] \end{aligned} \tag{A14}$$

while the analogous defined integral at the denominator is calculated as:

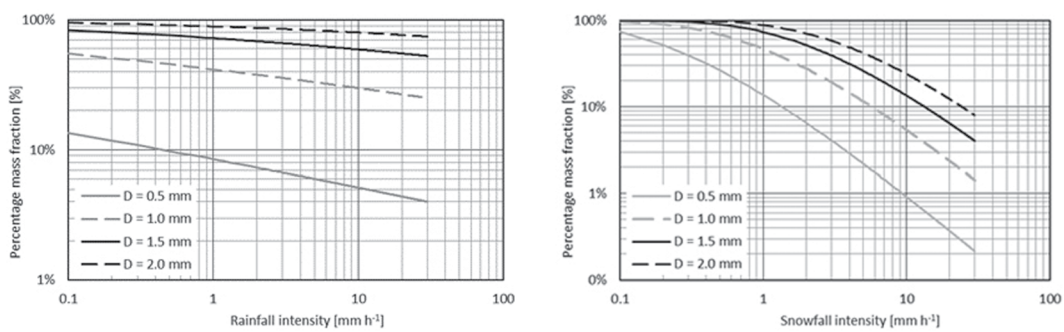

Figure A2. Percentage Mass Fraction of hydrometeors with the Precipitation Intensity (PI), PMF(PI), for liquid (left-hand panel) and solid (right-hand panel) precipitation with different diameters. Calculation is performed using the particle size distribution formulation shown in Equations A2–A4.

$$\mathrm{WC}_S = \frac{0.017\pi N_0}{6 \cdot 10^5}\left|\exp(-\lambda_0 D)\left(-\frac{D^2}{\lambda_0} - \frac{2D}{\lambda_0^2} - \frac{2}{\lambda_0^3}\right)\right|_0^\infty = \frac{0.017\pi N_0}{3\lambda_0^3 10^5} \tag{A15}$$

since when D tends to infinity:

$$\lim_{D\to\infty} \exp(-\lambda_0 D)\left(\lambda_0^2 D^2 + 2\lambda_0 D + 2\right) = 0 \tag{A16}$$

Therefore, the mass fraction for solid precipitation is easily obtained analytically as:

$$\mathrm{MF}_S(D) = 1 - \frac{\exp(-\lambda_0 D)\left(\lambda_0^2 D^2 + 2\lambda_0 D + 2\right)}{2} \tag{A17}$$

where λ_0 is a function of the snowfall intensity SI, as defined in Equation A4.

The Percentage Mass Fraction $\mathrm{PMF}_S(D)$ is plotted in Figure A1 (right-hand panel) over the range of equivolumetric particle diameters investigated in this work for different SI values, assuming $\lambda_0 = \lambda_0(\mathrm{SI})$ as proposed by Gunn and Marshall (1958). The PMF_S as a function of the snowfall intensity is instead plotted in Figure A2 (right-hand panel) for a few sample particle diameters.

The acronyms used throughout the manuscript are listed in Table A1.

Table A1
List of Acronyms

Acronym	Description
CFD	Computational Fluid Dynamics
CR	Catch Ratio
CWC	Collected Water Content
LPT	Lagrangian Particle Tracking
LTS	Local Time Stepping
LWC	Liquid Water Content
MF	Mass Fraction
NS	Navier-Stokes
NWC	Non-dimensional Water Content
OCE	Overall Collection Efficiency
OCR	Overall Catch Ratio
PI	Precipitation Intensity
PMF	Percentage Mass Fraction
PSD	Particle Size Distribution
RANS	Reynolds-averaged Navier–Stokes
RI	Rainfall Intensity
SI	Snowfall Intensity
SPICE	Solid Precipitation InterComparison Experiment
SST	Shear Stress Transport
STL	Standard Triangulation Language
URANS	Unsteady Reynolds Averaged Navier-Stokes
WC	Water Content
WMO	World Meteorological Organization

Data Availability Statement

Supplementary material including drawings of the investigated instruments, numerical schemes, flow velocity and drop trajectory maps and tables of the numerical catch ratios are available in Chinchella et al. (2023).

Acknowledgments
This work was developed in partial fulfillment of the PhD thesis work of E. Chinchella.

References

Alter, J. C. (1937). Shielded storage precipitation gages. *Monthly Weather Review*, *65*(7), 262–265. https://doi.org/10.1175/1520-0493(1937)65<262:SSPG>2.0.CO;2

Aqilah, F., Islam, M., Juretic, F., Guerrero, J., Wood, D., & Ani, F. N. (2018). Study of mesh quality improvement for CFD analysis of an airfoil. *IIUM Engineering Journal*, *19*(2), 203–212. https://doi.org/10.31436/iiumej.v19i2.905

Beard, K. V., & Chuang, C. (1987). A new model for the equilibrium shape of raindrops. *Journal of the Atmospheric Sciences*, *44*(11), 1509–1524. https://doi.org/10.1175/1520-0469(1987)044%3C1509:ANMFTE%3E2.0.CO;2

Caracciolo, C., Porcù, F., & Prodi, F. (2008). Precipitation classification at mid-latitudes in terms of drop size distribution parameter. *Advances in Geosciences*, *16*, 11–17. https://doi.org/10.5194/adgeo-16-11-2008

Cauteruccio, A., Brambilla, E., Stagnaro, M., Lanza, L. G., & Rocchi, D. (2021a). Experimental evidence of the wind-induced bias of precipitation gauges using Particle Image Velocimetry and particle tracking in the wind tunnel. *Journal of Hydrology*, *600*, 126690. https://doi.org/10.1016/j.jhydrol.2021.126690

Cauteruccio, A., Brambilla, E., Stagnaro, M., Lanza, L. G., & Rocchi, D. (2021b). Wind tunnel validation of a particle tracking model to evaluate the wind-induced bias of precipitation measurements. *Water Resources Research*, *57*(7), e2020WR028766. https://doi.org/10.1029/2020WR028766

Cauteruccio, A., Chinchella, E., Stagnaro, M., & Lanza, L. G. (2021). Snow particle collection efficiency and adjustment curves for the hotplate precipitation gauge. *Journal of Hydrometeorology*, *22*(4), 941–954. https://doi.org/10.1175/JHM-D-20-0149.s1

Cauteruccio, A., Colli, M., Freda, A., Stagnaro, M., & Lanza, L. G. (2020). The role of free-stream turbulence in attenuating the wind updraft above the collector of precipitation gauges. *Journal of Atmospheric and Oceanic Technology*, *37*(1), 103–113. https://doi.org/10.1175/JTECH-D-19-0089.1

Cauteruccio, A., Colli, M., Stagnaro, M., Lanza, L. G., & Vuerich, E. (2021). In situ precipitation measurements. In T. Foken (Ed.), *Handbook of atmospheric measurements (359-400)*. Springer Nature. https://doi.org/10.1007/978-3-030-52171-4_12

Cauteruccio, A., & Lanza, L. G. (2020). Parameterization of the collection efficiency of a cylindrical catching-type rain gauge based on rainfall intensity. *Water*, *12*(12), 3431. https://doi.org/10.3390/w12123431

Cauteruccio, A., Stagnaro, M., Lanza, L. G., & Chan, P. W. (2023). Adjustment of 1 min rain gauge time series using co-located drop size distribution and wind speed measurements. *Atmospheric Measurement Techniques*, *16*(17), 4155–4163. https://doi.org/10.5194/amt-16-4155-2023

CEN. (2010). *Hydrometry – Specification for a reference raingauge pit (EN 13798:2010)*. European Committee for Standardization (CEN).

Chen, G., Xiong, Q., Morris, P. J., Paterson, E. G., Sergeev, A., & Wang, Y. (2014). OpenFOAM for computational fluid dynamics. *Notices of the AMS*, *61*(4), 354–363. https://doi.org/10.1090/noti1095

Chinchella, E., Cauteruccio, A., & Lanza, L. (2023). Supplementary to "the overall collection efficiency of catching-type precipitation gauges in windy conditions" [Dataset]. Zenodo. https://doi.org/10.5281/zenodo.10033616

Chinchella, E., Cauteruccio, A., Stagnaro, M., & Lanza, L. G. (2021). Investigation of the wind-induced airflow pattern near the Thies LPM precipitation gauge. *Sensors*, *21*(14), 4880. https://doi.org/10.3390/s21144880

Chubb, T. H., Manton, M. J., Siems, S. T., Peace, A. D., & Bilish, S. P. (2015). Estimation of wind-induced losses from a precipitation gauge network in the Australian Snowy Mountains. *Journal of Hydrometeorology*, *16*(6), 2619–2638. https://doi.org/10.1175/JHM-D-14-0216.1

Colli, M., Lanza, L. G., Rasmussen, R. M., & Thèriault, J. M. (2016a). The collection efficiency of shielded and unshielded precipitation gauges. Part I: CFD airflow modelling. *Journal of Hydrometeorology*, *17*(1), 231–243. https://doi.org/10.1175/JHM-D-15-0010.1

Colli, M., Lanza, L. G., Rasmussen, R. M., & Thèriault, J. M. (2016b). The collection efficiency of shielded and unshielded precipitation gauges. Part II: Modelling particle trajectories. *Journal of Hydrometeorology*, *17*(1), 245–255. https://doi.org/10.1175/JHM-D-15-0011.1

Colli, M., Pollock, M., Stagnaro, M., Lanza, L. G., Dutton, M., & O'Connell, P. E. (2018). A Computational Fluid-Dynamics assessment of the improved performance of aerodynamic raingauges. *Water Resources Research*, *54*(2), 779–796. https://doi.org/10.1002/2017WR020549

Colli, M., Rasmussen, R. M., Thériault, J. M., Lanza, L. G., Baker, B. C., & Kochendorfer, J. (2015). An improved trajectory model to evaluate the collection performance of snow gauges. *Journal of Applied Meteorology and Climatology*, *54*(8), 1826–1836. https://doi.org/10.1175/JAMC-D-15-0035.1

Colli, M., Stagnaro, M., Lanza, L. G., Rasmussen, R., & Thériault, J. M. (2020). Adjustments for wind-induced undercatch in snowfall measurements based on precipitation intensity. *Journal of Hydrometeorology*, *21*(5), 1039–1050. https://doi.org/10.1175/JHM-D-19-0222.1

Duchon, C. E., & Essenberg, G. R. (2001). Comparative rainfall observations from pit and aboveground rain gauges with and without wind shields. *Water Resources Research*, *37*(12), 3253–3263. https://doi.org/10.1029/2001WR000541

Folland, C. K. (1988). Numerical models of the raingauge exposure problem, field experiments and an improved collector design. *Quarterly Journal of the Royal Meteorological Society*, *114*(484), 1485–1516. https://doi.org/10.1002/qj.49711448407

Gunn, K. L. S., & Marshall, J. S. (1958). The distribution with size of aggregate snowflakes. *Journal of Meteorology*, *15*(5), 452–461. https://doi.org/10.1175/1520-0469(1958)015<0452:TDWSOA>2.0.CO;2

Hoover, J., Earle, M. E., Joe, P. I., & Sullivan, P. E. (2021). Unshielded precipitation gauge collection efficiency with wind speed and hydrometeor fall velocity. *Hydrology and Earth System Sciences*, *25*(10), 5473–5491. https://doi.org/10.5194/hess-25-5473-2021

Jeanmasson, G., Mary, I., & Mieussens, L. (2019). On some explicit local time stepping finite volume schemes for CFD. *Journal of Computational Physics*, *397*, 108818. https://doi.org/10.1016/j.jcp.2019.07.017

Jevons, W. S. (1861). On the deficiency of rain in an elevated rain-gauge, as caused by wind. *The London, Edinburgh and Dublin Philosophical Magazine and Journal of Science*, *21*(4), 421–433. https://doi.org/10.1080/14786446108643180

Jones, W. P., & Launder, B. E. (1972). The prediction of laminarization with a two-equation model of turbulence. *International Journal of Heat and Mass Transfer*, *15*(2), 301–314. https://doi.org/10.1016/0017-9310(72)90076-2

Khvorostyanov, V. I., & Curry, J. A. (2005). Fall velocities of hydrometeors in the atmosphere: Refinements to a continuous analytical power law. *Journal of the Atmospheric Sciences*, *62*(12), 4343–4357. https://doi.org/10.1175/JAS3622.1

Kochendorfer, J., Nitu, R., Wolff, M., Mekis, E., Rasmussen, R., Baker, B., et al. (2018). Testing and development of transfer functions for weighing precipitation gauges in WMO-SPICE. *Hydrology and Earth System Sciences*, *22*(2), 1437–1452. https://doi.org/10.5194/hess-22-1437-2018

Kochendorfer, J., Rasmussen, R., Baker, B., Landolt, A., Smith, C., Earle, M., et al. (2022). How well are we measuring snow post-SPICE? *Bulletin of the American Meteorological Society*, *103*(2), E370–E388. https://doi.org/10.1175/BAMS-D-20-0228.1

Koshmieder, H. (1934). Methods and results of definite rain measurements. *Monthly Weather Review*, *62*(1), 5–7. https://doi.org/10.1175/1520-0493(1934)62<5:MARODR>2.0.CO;2

Kurtyka, J. C. (1953). *Precipitation measurements study* (Rep. of Investigation No. 20) (pp. 179). State Water Survey Division.

Leroux, N. R., Thériault, J. M., & Rasmussen, R. (2021). Improvement of snow gauge collection efficiency through a knowledge of solid precipitation fall speed. *Journal of Hydrometeorology*, *22*(4), 997–1006. https://doi.org/10.1175/JHM-D-20-0147.1

Liu, F. (2016). A thorough description of how wall functions are implemented in OpenFOAM. In H. Nilsson (Ed.), *Proceedings of CFD with OpenSource software* (Vol. 34). Chalmers University of Technology. Retrieved from https://www.tfd.chalmers.se/~hani/kurser/OS_CFD_2016/FangqingLiu/openfoamFinal.pdf

Marshall, J. S., & Palmer, W. M. (1948). The distribution of raindrops with size. *Journal of Meteorology*, *5*(4), 165–166. https://doi.org/10.1175/1520-0469(1948)005<0165:TDORWS>2.0.CO;2

Masuda, M., Yatagai, A., Kamiguchi, K., & Tanaka, K. (2019). Daily adjustment for wind-induced precipitation undercatch of daily gridded precipitation in Japan. *Earth and Space Science*, *6*(8), 1469–1479. https://doi.org/10.1029/2019EA000659

Meikle, H. (1819). On the different quantities of rain collected in rain-gauges at different heights. *Annals of Philosophy*, *14*, 312–313. Retrieved from https://www.biodiversitylibrary.org/page/15876756

Menter, F. R. (1994). Two-equation eddy-viscosity turbulence models for engineering applications. *Journal of the American Institute of Aeronautics and Astronautics (AIAA)*, *32*(8), 1598–1605. https://doi.org/10.2514/3.12149

Menter, F. R., Kuntz, M., & Langtry, R. (2003). Ten years of industrial experience with the SST turbulence model. In K. Hanjalic, Y. Nagano, & M. Tummers (Eds.), (Eds), *Turbulence, heat and mass transfer* (Vol. 4, No. (1), pp. 625–632). Begell House Inc.

Muchan, K., & Dixon, H. (2019). Insights into rainfall undercatch for differing raingauge rim heights. *Hydrology Research*, *50*(6), 1564–1576. https://doi.org/10.2166/nh.2019.024

Mueller, C. C., & Kidder, E. H. (1972). Rain gage catch variation due to airflow disturbances around a standard rain gage. *Water Resources Research*, *8*(4), 1077–1082. https://doi.org/10.1029/WR008i004p01077

Nešpor, V., Krajewski, W. F., & Kruger, A. (2000). Wind-induced error of raindrop size distribution measurement using a two-dimensional video disdrometer. *Journal of Atmospheric and Oceanic Technology*, *17*(11), 1483–1492. https://doi.org/10.1175/1520-0426(2000)017<1483:WIEORS>2.0.CO;2

Nešpor, V., & Sevruk, B. (1999). Estimation of wind-induced error of rainfall gauge measurements using a numerical simulation. *Journal of Atmospheric and Oceanic Technology*, *16*(4), 450–464. https://doi.org/10.1175/1520-0426(1999)016<0450:EOWIEO>2.0.CO;2

Nitu, R., Roulet, Y.-A., Wolff, M., Earle, M., Reverdin, A., Smith, C., et al. (2018). *WMO solid precipitation Intercomparison experiment (2012 - 2015)* (WMO instruments and observing methods report No. 131). World Meteorological Organization. Retrieved from https://library.wmo.int/records/item/56317-wmo-solid-precipitation-intercomparison-experiment-spice-2012-2015

OpenFoam. (2020). OpenCFD release OpenFOAM® v2012 (20 12) [Software]. Stl. Retrieved from https://www.openfoam.com/news/main-news/openfoam-v20-12

Pollock, M., O'Donnell, G., Quinn, P., Dutton, M., Black, A., Wilkinson, M., et al. (2018). Quantifying and mitigating wind-induced undercatch in rainfall measurements. *Water Resources Research*, *54*(6), 3863–3875. https://doi.org/10.1029/2017WR022421

Rasmussen, R., Baker, B., Kochendorfer, J., Meyers, T., Landolt, S., Fischer, A. P., et al. (2012). How well are we measuring snow: The NOAA/FAA/NCAR winter precipitation test bed. *Bulletin of the American Meteorological Society*, *93*(6), 811–829. https://doi.org/10.1175/BAMS-D-11-00052.1

Rasmussen, R., Vivekanandan, J., Cole, J., Masters, B. M. C., & Masters, C. (1999). The estimation of snowfall rate using visibility. *Journal of Applied Meteorology*, *38*(10), 1542–1563. https://doi.org/10.1175/1520-0450(1999)038%3C1542:TEOSRU%3E2.0.CO;2

Reynolds, O. (1895). On the dynamical theory of incompressible viscous fluids and the determination of the criterion. *Philosophical Transactions of the Royal Society of London. A*, *186*, 123–164. https://doi.org/10.1098/rspa.1995.0116

Rodda, J. C., & Dixon, H. (2012). Rainfall measurement revisited. *Weather*, *67*(5), 131–136. https://doi.org/10.1002/wea.875

Rodda, J. C., & Smith, S. W. (1986). The significance of the systematic error in rainfall measurement for assessing wet deposition. *Atmospheric Environment*, *20*(5), 1059–1064. https://doi.org/10.1016/0004-6981(86)90293-3

Sevruk, B. (1982). *Methods of correction for systematic error in point precipitation measurement for operational use (Rep. n. 589)* (Operational Hydrology Rep. n. 21) (pp. 106). World Meteorological Organization. Retrieved from https://library.wmo.int/doc_num.php?explnum_id=1238

Smith, C. D., Mekis, E., Hartwell, M., & Ross, A. (2022). The hourly wind-bias-adjusted precipitation data set from the Environment and Climate Change Canada automated surface observation network (2001–2019). *Earth System Science Data*, *14*(12), 5253–5265. https://doi.org/10.5194/essd-14-5253-2022

Spalding, D. B. (1961). A single formula for the law of the wall. *Journal of Applied Mechanics*, *28*(3), 455–458. https://doi.org/10.1115/1.3641728

Thériault, J. M., Rasmussen, R., Ikeda, K., & Landolt, S. (2012). Dependence of snow gauge collection efficiency on snowflake characteristics. *Journal of Applied Meteorology and Climatology*, *51*(4), 745–762. https://doi.org/10.1175/JAMC-D-11-0116.1

Thériault, J. M., Rasmussen, R., Petro, E., Trépanier, J. Y., Colli, M., & Lanza, L. G. (2015). Impact of wind direction, wind speed, and particle characteristics on the collection efficiency of the double fence intercomparison reference. *Journal of Applied Meteorology and Climatology*, *54*(9), 1918–1930. https://doi.org/10.1175/JAMC-D-15-0034.1

Uijlenhoet, R., & Torres, D. S. (2006). Measurement and parameterization of rainfall microstructure. *Journal of Hydrology*, *328*(1–2), 1–7. https://doi.org/10.1016/j.jhydrol.2005.11.038

Utsumi, N., Kanae, S., Kim, H., Seto, S., Oki, T., Nitta, T., & Hirabayashi, Y. (2008). Importance of wind-induced undercatch adjustment in a gauge-based analysis of daily precipitation over Japan. *Hydrological Research Letters*, *2*, 47–51. https://doi.org/10.3178/hrl.2.47

Wilcox, D. C. (1988). Reassessment of the scale-determining equation for advanced turbulence models. *Journal of the American Institute of Aeronautics and Astronautics (AIAA)*, *26*(11), 1299–1310. https://doi.org/10.2514/3.10041

Wolff, M. A., Isaksen, K., Petersen-Øverleir, A., Ødemark, K., Reitan, T., & Brækkan, R. (2015). Derivation of a new continuous adjustment function for correcting wind-induced loss of solid precipitation: Results of a Norwegian field study. *Hydrology and Earth System Sciences*, *19*(2), 951–967. https://doi.org/10.5194/hess-19-951-2015

Yang, D., Elomaa, E., Tuominen, A., Aaltonen, A., Goodison, B., Gunther, T., et al. (1999). Wind-induced precipitation undercatch of the Hellmann gauges. *Nordic Hydrology*, *30*(1), 57–80. https://doi.org/10.2166/nh.1999.0004